XI. Solid Propellant Engineering

PROPULSION DIVISION

A. Interior Ballistic Design and Experimental Development of a Self-Obturating, Propellant-Actuated Device, O. K. Heiney

1. Introduction

A ballistic launcher capable of deploying a sampling device to a location reasonably remote from a landed vehicle is a potential requirement for proposed future planetary landing systems. Remote deployment would be employed to acquire chemical or mineral specimens uncontaminated by either the presence of the lander or its retro-rocket plume impingement. Device design would be conventional and straightforward except for two additional required characteristics: (1) the system must be self-obturating subsequent to payload ejection, and (2) the system must be compatible with the sterilization requirement. Self-obturation is necessary to prevent (1) possible degradation of the landed vehicle's optical surfaces, and (2) additional area chemical contamination due to combustion products and ejecta associated with ballistic firings.

2. System Design

a. Propellant. The sterilization requirement is satisfied if a squib and main charge propellant combination can undergo six 56-hr sterilization cycles at 275°F. Surplus squibs from the *Surveyor* program were found to perform adequately after exposure to this environment.

The first main charge propellant investigated, Hercules 8028, was found to be adequate for this application. The propellant, developed during government-funded programs at Hercules, was designed to perform subsequent to extended exposure to high temperatures. It is a rubber-based composite formulation utilizing HMX as the oxidizer. The propellant demonstrates a weight loss of less than 1% and a trace of minor surface discoloration subsequent to exposure to the standard sterilization cycle. Externally, the individual propellant grains did not appear to have been physically degraded; however, the interior ballistic performance of the cycled propellant indicated internal degradation had occurred. This increased tendency of the grains to fragment during the ballistic cycle, although annoying, did not materially inhibit the usefullness of the propellant.

b. Launcher. The purpose of the launcher is to project an approximately 2-lb claw to acquire a sample which will be returned to the lander and subjected to chemical analysis. For experimental ballistic development, an inert cylinder was used to simulate a retrievable claw. Optimum ballistic design indicated the necessary muzzle velocity of

120 ft/s could best be obtained with a 60 caliber device having a 6-in. stroke. The main charge is 0.8 g of propellant with a web of 0.0048 fired in an initial chamber volume of 0.50 in. The device develops a peak pressure in the area of 5,000 lb. Since it is a requirement that all combustion products be sealed in the bore, a dual development approach was used. A simple lead slug obturation system and a more sophisticated tapered slug and sleeve approach were attempted.

In the lead slug system, shown in Fig. 1a, the payload, D, is propelled down the bore by means of gas pressure on an obturator, A. At stroke completion, the obturator is swaged onto a retainer, B, which is held to the barrel by a locking lug, C. The juncture of the lead obturator and the retainer provides a positive and total gas and debris seal. Subsequent to firing, retained pressure was vented by cracking a relief valve, E, which would not be employed on an operational system. Through a series of firings with sterilized and unsterilized components, this device invariably held the pressure and sealed in all combustion products.

The sliding sleeve system, shown in Fig. 1b, employed a tapered steel projector, F, which, at cycle termination, interfered with, and was stopped by, a tapered aluminum

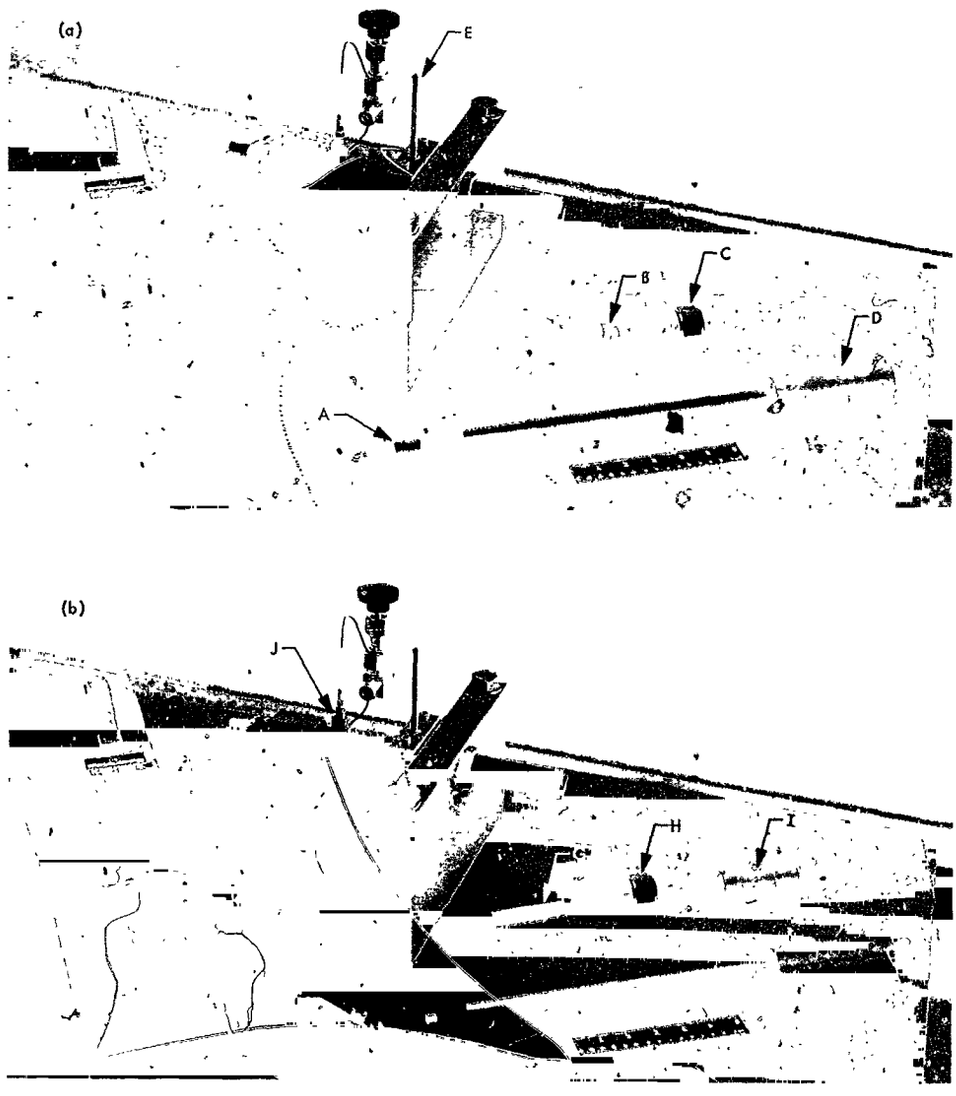

Fig. 1. Ballistic launcher components for: (a) lead-seal and (b) sliding-sleeve systems

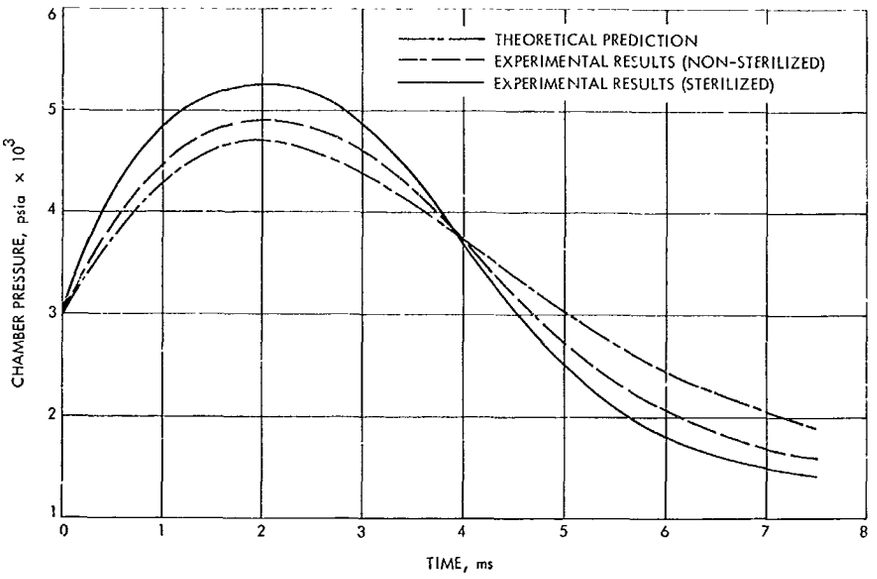

Fig. 2. Theoretical and experimental pressure–time plots

cylinder, G, held in a locking sleeve, I, and retained by a lock nut, H. This system was also effective for holding pressure; however, after several firings the projector became scored and would bleed off gases over a period of several minutes. This would not occur in an operational device since a new projector would be used for each firing.

Pressures were recorded by a Kistler piezometric pressure transducer, J, which fed a charge amplifier, K. The theoretical interior ballistics developed from previous analysis (SPS 37-43, Vol. IV, pp. 167–170) and coded for a digital computer is compared with experimental results and shown in Fig. 2. Note that both sterilized and non-sterilized firings exhibited higher peak pressures than were theoretically predicted. This is due to the squib fracturing a percentage of the propellant grains. For the sterilized system, the effect is more pronounced due to the minor structural degradation experienced during thermal cycling.

Both obturation mechanisms are acceptable and positive, with the lead seal technique being simpler and possibly somewhat more effective.

B. T-Burner Studies, *E. H. Perry*

1. Introduction

The T-burner is, perhaps, the most widely used device for studying combustion instability in solid propellants despite the fact that several important questions surrounding T-burner technique remain unanswered. These questions concern both the possible effects of the T-burner itself on the phenomena under examination, and the equivalence of the various methods of conducting T-burner experiments. Some 200 test firings have now been completed in JPL burners in order to resolve some of these questions and provide a higher level of confidence for future T-burner experiments.

2. Burner and Methods Description

The T-burner, shown in Fig. 3, is a centrally vented cylindrical cavity containing a disk of solid propellant in

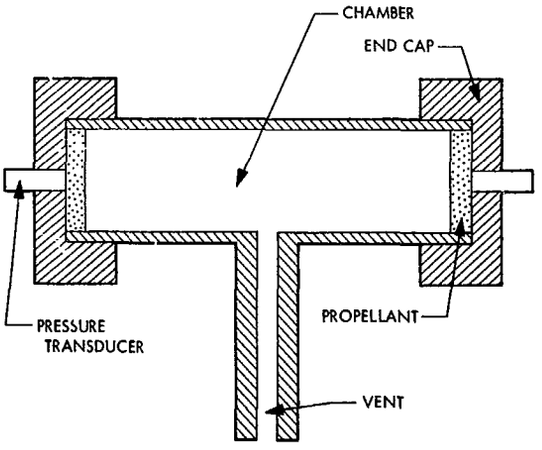

Fig. 3. Cross-sectional view of the T-burner

each end. As the propellant burns, pressure oscillations driven by the burning surface develop in the chamber. These oscillations, observed with pressure transducers behind the propellant, grow exponentially until a limiting amplitude is reached. Remaining near this amplitude until burnout occurs, they then decay exponentially because of losses present in the chamber.

The frequency of the oscillations is controlled by the length of the chamber since, in practice, only the fundamental acoustic mode of the cavity is observed. Frequencies ranging from 250–6000 Hz were obtained in the present experiments by using chambers with lengths varying from 43.5–3.25 in.

The ability of the burning surface to drive such oscillations is measured in terms of the "response function" of the propellant. Knowledge of the response function is the main goal of T-burner experiments since such information permits a calculation of the stability characteristics of a full-scale rocket motor using the same propellant. For a given propellant, the response function depends on mean chamber pressure, initial grain temperature, and the frequency of the oscillations.

Presently, there are two methods, often referred to as the "growth–decay" and "variable-area" methods, of conducting T-burner tests to determine the response function. Using the growth–decay method, one measures how rapidly the oscillations grow during the initial portion of the test and also how rapidly they decay after burnout. The decay rate provides a measure of the losses in the chamber, which are assumed to remain constant during the entire test. Allowing for these losses, one can then calculate how rapidly the oscillations would grow if driven by the burning surface in a lossless chamber. The response function is deduced from these calculations.

In the variable-area method, one measures only how rapidly the oscillations grow. However, in this case the propellant disk covers only a portion of the total cross-sectional area of the chamber. By measuring the growth rate as a function of this area ratio, the response function can be deduced. Further details of these methods are given in Ref. 1.

3. Experimental Comparison of the Two Methods

A comparison of the results obtained by the two methods for the same propellant was undertaken in the present experiments. The propellant used was a PBAN/AP composite, denoted as A-13, supplied by the Naval Weapons Center at China Lake, California. A chamber diameter of 1.5 in., a mean chamber pressure of 315 psia, and an initial grain temperature of 90° F were used in all the tests. For the variable-area tests, area ratios of 1.00, 0.75, and 0.43 were used. Kistler model 603A pressure transducers were used to observe the pressure oscillations in these tests as well as in the others to be discussed later.

The response function determined from these experiments is shown in Fig. 4 as a function of frequency. The upper curve represents values calculated from growth–decay measurements and the lower curve those calculated

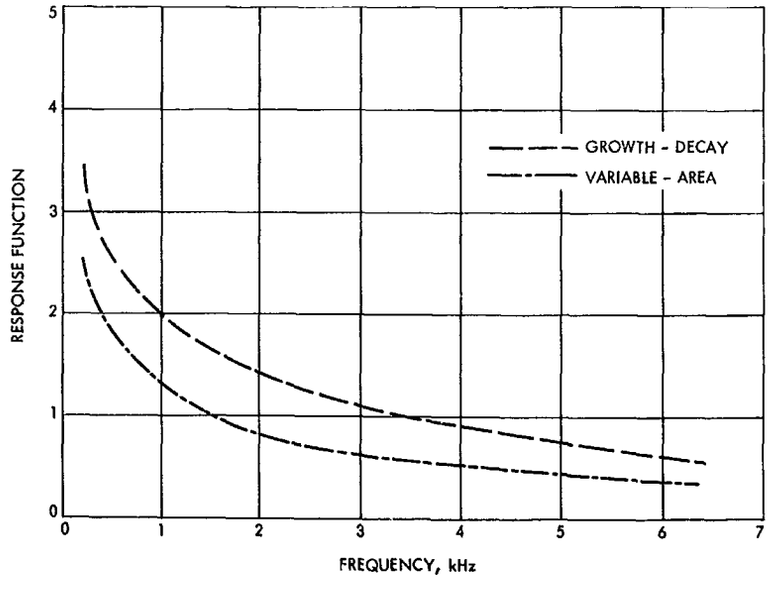

Fig. 4. Response function determined by the two T-burner methods

from variable-area measurements. The poor agreement of the two curves indicates that the two methods of conducting T-burner experiments are not equivalent. Unfortunately, there is no way to determine from these tests which, if either, of the two methods yields correct values for the response function. However, considering the underlying assumptions of the two methods and their relative experimental difficulties, one is inclined to favor the growth–decay method. However, such considerations cannot be taken as conclusive at this time.

4. Effects of Chamber Diameter

Regardless of which method is used, it is clear that the burner itself should have no effect on the response function of the propellant if meaningful results are to be obtained. To determine possible effects of chamber diameter on the response function, values for the A-13 propellant were obtained from tests conducted in burners of different diameter. The growth–decay method was adopted for these tests, and burner diameters of 1.0, 1.5, and 2.5 in. were used. Figure 5 shows the response function determined from these experiments as a function of frequency. It is apparent from these results that the chamber diameter has no effect on response function measurements. This is, perhaps, the most significant, as well as encouraging, fact to emerge from the experiments, since the presence of such effects would greatly reduce the credibility of T-burner results. Thus, it appears that discrepancies among various laboratories on reported values of response functions cannot be attributed to differences in burner diameter, but rather to other, perhaps more subtle, aspects of the test.

5. Comparison of Ignition Procedures

One such aspect is the procedure used for igniting the propellant. For these tests, the normal method was to cover the entire face of the propellant disk with a pyrotechnic igniter paste. Ignition was brought about by passing an electric current through a Nichrome wire in contact with this paste. This method appeared to provide a rapid, simultaneous ignition of both propellant disks in the chamber and resulted in burn times consistent with the known burning rate of the propellant.

In some 30 tests, however, a procedure was followed in which the igniter paste covered only a small portion of the propellant disk. These "spot igniter" tests all had burn times considerably longer than the normal tests, providing perhaps the best evidence that a poor ignition had occurred. More important, however, were the lower rates of growth and decay of the pressure oscillations that accompanied the longer burn times. As a result, the response function calculated from these tests was correspondingly lower. The lower oscillation growth rate was probably due to uneven burning of the propellant, and the lower decay rate due to uneven burnout of the two disks. In any case, it is now evident that ignition procedures can play a rather substantial role in T-burner experiments and should be given careful consideration.

6. Chamber Losses

It is rather apparent that an understanding of the chamber losses is necessary for a complete understanding of the burner. Although the present experiments provide

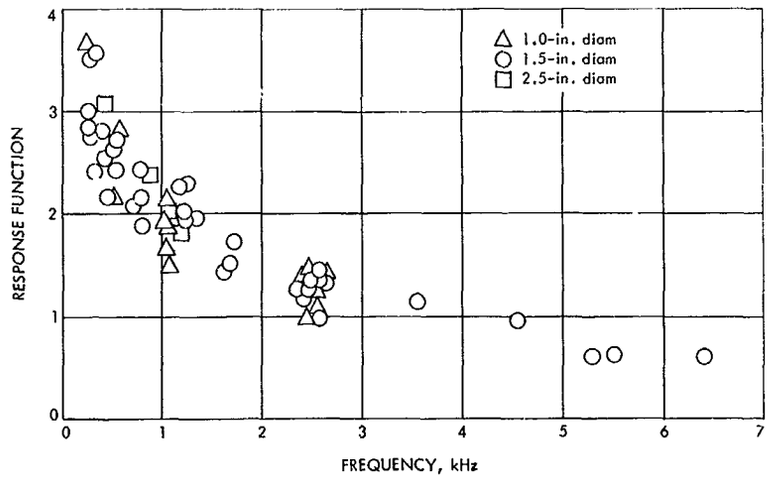

Fig. 5. Response function determined by T-burners of different diameters

some new insights into the nature of these losses, a true understanding of them is still lacking.

The rate of decay of the oscillations after burnout provides a measure of the chamber losses and is measured in terms of a chamber "decay constant." It has generally been assumed that the decay is due to viscous and thermal dissipation at the chamber walls. If this were the case, the losses would be the familiar Kirchkoff–Helmholtz losses of classical acoustics which are proportional to the square root of the frequency and inversely proportional to the chamber diameter. Figure 6 shows decay constants for the three chamber diameters mentioned earlier as a function of frequency. There are two aspects of the losses that are apparent from the figure: (1) the losses increase approximately as the square root of the frequency, as indicated by the dashed line, and (2) the losses show no dependence on chamber diameter.

The latter fact indicates that even though the Kirchkoff–Helmholtz losses are undoubtedly present, other losses either dominate them or at least offset their diameter dependence. Reference 2 provides experimental evidence that large amplitude sound waves are attenuated more strongly than the small amplitude waves generally treated in linear acoustic theory. Since the pressure oscillations present in T-burners are typically very large amplitude waves, the observed chamber losses could arise from such "finite amplitude" effects. However, until further work is done, these are offered only as a possible explanation.

References

1. Beckstead, M. W., and Culick, F. E. C., *A Comparison of Analysis and Experiment for Solid Propellant Combustion Instability*, Technical Publication 4531. Naval Weapons Center, China Lake, Calif., May 1968.
2. Lehmann, K. O., *"Die Dampfungsverluste bei Starken Schallschwingungen in Rohren,"* *Ann. Phys.*, Vol. 21, pp. 533–552, 1934.

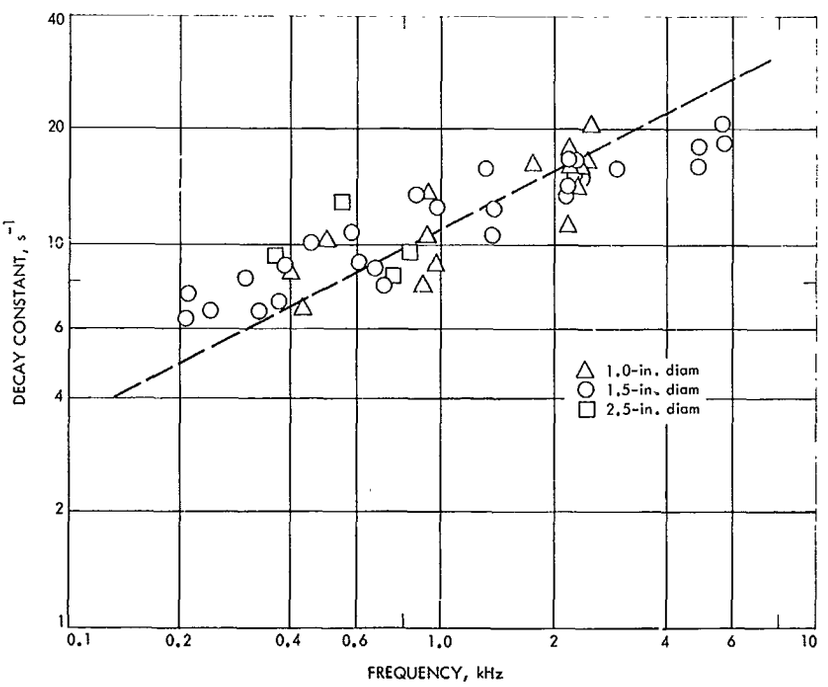

Fig. 6. Chamber decay constants for different diameter burners

XII. Polymer Research

PROPULSION DIVISION

A. A Model for the Effect of Dewetting on Mechanical Behavior of Composites Based on a Parabola-Shaped Void Cavity,

R. F. Fedors and R. F. Landel

1. Introduction

In a previous article (SPS 37-41, Vol. IV, pp. 97–107), a model was proposed which enabled one to relate the stress–strain behavior to the volume dilation, i.e., void formation, for composites which undergo significant strain-induced particle–binder dewetting. It was also demonstrated that the model provided satisfactory agreement with experimental data for SBR[1]–glass bead composites.

The formation of voids leads to two directly observable effects: (1) a relatively large strain-induced dilation, which is a consequence of the formation and growth of voids, and (2) a modified stress–strain response, which is assumed to be related to the continuous decrease, as the voids increase in size, in the fraction of the particle surface area which remains in contact with the binder; it is this latter effect which causes the stress at a given strain level to be lower than it would be in the absence of dewetting. A limit is reached, however, when dewetting occurs to such an extent that the particle surface is essentially no longer in contact with the binder, in which case the stress–strain response of the composite approaches the response of the unfilled binder.

[1]SBR = styrene–butadiene rubber.

In developing the model, it was assumed that the voids formed were cone-shaped. However, one difficulty of the cone-shaped void is the existence of a discontinuity at the apex of the cone. While such a discontinuity does not affect the calculation of the void volume as a function of the strain or of the fraction of particle surface area remaining in contact with the binder, it may pose problems in other related kinds of calculations, e.g., in stress analysis applications.

For this reason, the previous study has been extended to a consideration of a void having a more realistic parabolic shape, and the purpose of this article is to present these new results.

2. Discussion

a. Development of the model. As in the previous article, we consider a single spherical filler particle imbedded in a binder matrix. Before any strain is imposed on the system, the particle surface is assumed to be completely wetted by the binder as indicated schematically in Fig. 1a. When the composite is strained, dewetting is assumed to occur with the resultant formation of a parabola-shaped cavity on each side of the particle, parallel to the strain axis as indicated in Fig. 1b.

The center of the spherical particle of radius r is located at the origin of a set of x, y, z coordinate axes. The void volume will then consist of the enclosed volume formed

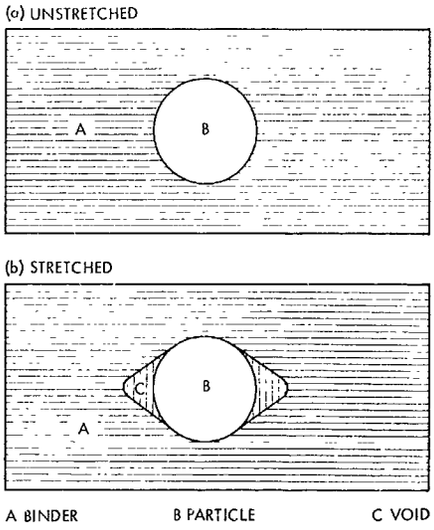

Fig. 1. Schematic representation of a spherical filler particle imbedded in an elastomeric binder

by the intersection of a paraboloid of revolution with a circle of revolution, i.e., a sphere. The dewetted surface area of the particle is then taken as the spherical surface in contact with the void volume. Both the void volume and dewetted surface area will be symmetric with respect to the x-axis and, hence, one can consider the simpler two-dimensional case of the intersection of a circle with a parabola. The quantities of interest are then obtained by permitting both the circle and parabola to revolve about the x-axis.

Figure 2 shows a circle of radius r, with center located at the origin of the x, y axes, intersecting with a parabola symmetrical with respect to the x-axis. The equation of the circle is simply

$$x^2 + y^2 = r^2 \tag{1}$$

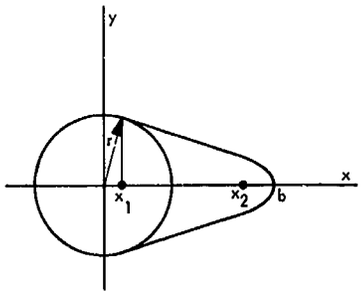

Fig. 2. Details of the parabolic void cavity

We require the parabolic void to simultaneously intersect and be tangent to the circle in the interval $0 \leq x \leq r$, say at the point (x_1, y_1) when the focus of the parabola is at the point $(x_2, 0)$. Further, as x_2 increases, i.e., as the void increases in size, the point of intersection on the x-axis decreases to a limiting value of zero. Because of symmetry, the form of the family of parabolas is taken as

$$y^2 = B(b - x) \tag{2}$$

where B and b are parameters. When $y = 0, x = b$, which represents the maximum separation of the binder from the filler particle. Hence, b $(b \geq r)$ will be referred to as the "length" of the parabolic void, which, as will be shown later, depends directly on the strain. At a fixed value of b, the parameter B is uniquely defined by the condition that the tangent of both the sphere and paraboloid be equal at each point of intersection. Thus, based on this requirement, it is easy to show that the x value at the point of intersection is $B/2$ and further that B is related to b by

$$B = 2\left[b - (b^2 - r^2)^{1/2}\right] \tag{3}$$

Hence, the family of parabolas which define the void shape is given by

$$y^2 = 2[b - (b^2 - r^2)^{1/2}]\,(b - x) \tag{4}$$

At any value of the parabola "length" b, the fraction of particle surface area remaining in contact with the binder, S_a, is

$$S_a = \frac{x_1}{r} \tag{5}$$

since dewetting is assumed to occur on both sides of the particle.

Only that fraction of the filler which remains in contact with the binder will alter the stress-strain response of the system and, hence, the initial volume loading of filler before dewetting ϕ_0 will, in effect, be reduced according to the fraction of particle surface area enclosed within the void volume. On this basis, the effective volume fraction of filler ϕ_{eff} is given by

$$\phi_{eff} = \frac{\phi_0 x_1}{r} \tag{6}$$

It is assumed, as before, that the separation of the parabola from the particle surface $(b - r)$ is directly proportional to the particle radius and to the effective strain,

which is taken to be the difference between the internal strain ϵ_i and the threshold value ϵ_{i_0} required to initiate dewetting, i.e.,

$$(b - r) = k_1 r(\epsilon_i - \epsilon_{i_0}) \tag{7}$$

where k_1 is a constant whose magnitude depends on the strength of the filler–binder interaction.

The internal strain is the strain experienced by the binder when an external or overall strain ϵ is imposed on the composite. The relationship between ϵ and ϵ_i can be taken either as

$$\epsilon_i = \frac{\epsilon}{1 - \phi_0^{1/3}} \tag{8}$$

or as

$$\epsilon_i = \frac{\epsilon}{1 - \phi_0} \tag{9}$$

depending on the assumption made concerning the manner in which the particles are considered to pack. The latter representation, Eq. (9), is probably a more adequate approximation. Returning to Eq. (6), ϕ_{eff} can now be written as

$$\phi_{eff} = \phi_0[(C_1 + 1) - (C_1^2 + 2C_1)^{1/2}] \tag{10}$$

where

$$C_1 = k_1 \epsilon_{eff}$$

and ϵ_{eff} is either

$$\frac{\epsilon - \epsilon_0}{1 - \phi_0^{1/3}} \quad \text{or} \quad \frac{\epsilon - \epsilon_0}{1 - \phi_0}$$

as the case may be. This equation can be compared to the expression derived on the assumption of a cone-shaped void,

$$\phi_{eff} = \frac{\phi_0}{1 + C} \tag{11}$$

where $C = k\epsilon_{eff}$. It is expected that $k_1 \neq k$.

b. Calculation of the void volume. If the void volume per particle is taken as twice the volume of the paraboloid of revolution having a spherical segment as a base, then the relative volume change as a function of the strain is given by

$$\frac{\Delta V}{V_0} = \frac{1}{V_0} \sum_{i=1}^{N} \frac{2\pi n_i r_i^3}{3} \times \{C_1[(C_1 + 2)(C_1^2 + 2C_1)^{1/2} - C_1(C_1 + 3)]\} \tag{12}$$

where n_i is the number of particles of radius r_i and N is the total number of particles present. If the particles are assumed to be monodisperse, then Eq. (12) reduces to

$$\frac{\Delta V}{V_0} = \frac{\phi_0}{2} \{C_1[(C_1 + 2)(C_1^2 + 2C_1)^{1/2} - C_1(C_1 + 3)]\} \tag{13}$$

which may be compared to the result derived on the basis of a cone-shaped cavity,

$$\frac{\Delta V}{V_0} = \frac{\phi_0}{2}\left(\frac{C^2}{1 + C}\right) \tag{14}$$

Figure 3 shows a comparison of these equations in the form $2\Delta V/\phi_0 V_0$ versus either C or C_1. Curves 1 and 2 show the behavior of Eq. (13) and (14), respectively, assuming $C = C_1$. As expected, the parabolic void yields a larger value for the volume dilatation at a given strain than does the cone-shaped void. However, there is no *a priori* reason to expect the k values (and hence the C values) will be the same for each model. If one takes $k_1 = 1.93\ k$ ($C_1 = 1.93\ C$), then the dashed curve 3 is obtained, which indicates that in the region of interest,

$$0 \leq \frac{2\Delta V}{\phi_0 V_0} \sim 1.4$$

the two expressions do not markedly differ. The parabolic model predicts a somewhat larger volume increase at small strains and a somewhat smaller increase at large strains than does the cone model. It is probable that either equation can be used to represent experimental data over limited ranges.

c. Effect of dewetting on the modulus. The modulus of a composite, E, in the absence of dewetting can be represented by an equation of the form (SPS 37-41, Vol. IV)

$$\frac{E}{E_0} = \left(\frac{\phi_m}{\phi_m - \phi_0}\right)^n \tag{15}$$

where E_0 is the modulus of the binder, ϕ_m is the maximum volume fraction of filler which the binder can accept, and

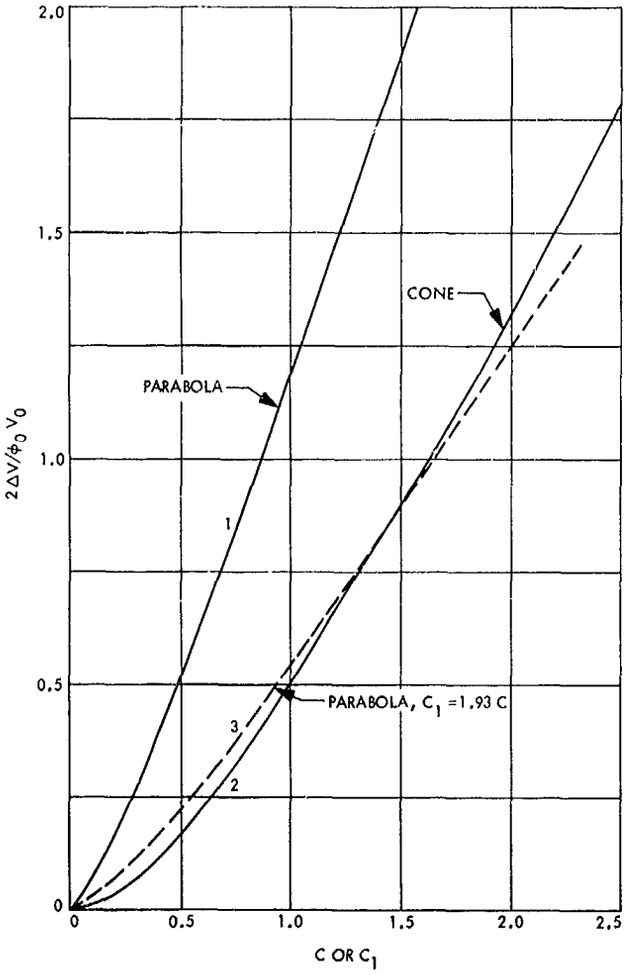

Fig. 3. Comparison of the volume dilatation–strain response for both the cone and parabola model

n has the value 2 or 2.5. When dewetting occurs, Eq. (15) is still assumed to apply, provided ϕ_0 is replaced by ϕ_{eff}. For the parabolic model, the modulus is given by

$$\frac{E}{E_0} = \left\{\frac{\phi_m}{\phi_m - \phi_0\left[(C_1 + 1) - (C_1^2 + 2C_1)^{1/2}\right]}\right\}^n \quad (16)$$

which may be compared to the result obtained from the cone model,

$$\frac{E}{E_0} = \left[\frac{\phi_m}{\phi_m - \left(\frac{\phi_0}{1 + C}\right)}\right]^n \quad (17)$$

These equations are compared in Fig. 4 in the form E/E_0 versus C or C_1. The value of ϕ_m was taken equal to 0.63,

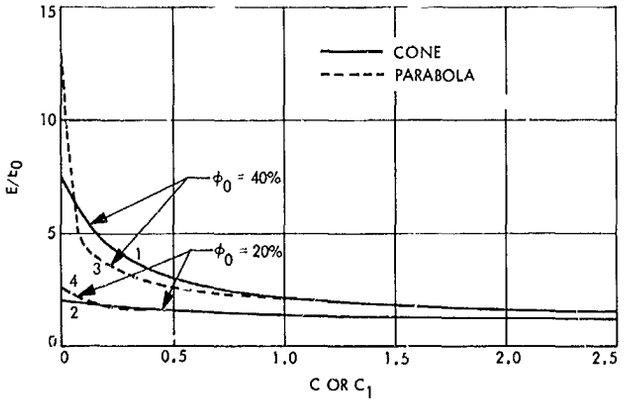

Fig. 4. Comparison of the modulus of a composite as a function of strain for both the cone and parabola model

which is typical for large-size spheres. Values of $\phi_0 = 0.2$ and 0.4 were also used. Previous results (SPS 37-41, Vol. IV) have shown that Eq. (17) adequately describes experimental stress–strain data obtained with SBR–glass bead composites, provided n is set equal to 2 and curves 1 and 2 show the behavior of Eq. (17) for $\phi_0 = 0.4$ and 0.2, respectively. Curves 3 and 4 represent the behavior predicted by Eq. (16) for $\phi_0 = 0.4$ and 0.2, respectively, when n is set equal to 2.5 rather than 2 and C_1 is taken equal to 1.93 C. Comparing curves 1 and 3 for $\phi_0 = 0.2$, it is apparent that the difference is negligible for C_1 or $C > 0.1$. For $\phi_0 = 0.4$, there is a greater divergence, especially for small C_1 or C values, which corresponds to systems at very small strains and/or systems having small k or k_1 values. Reliable data in this region are required to ascertain which model is the more correct. However, for C or $C_1 > 0.5$, the two equations differ at most by only about 6%, and at larger C values, the difference is negligible. Hence, for the SBR–glass bead system, it appears that either model can be employed to describe the stress–strain behavior.

B. Investigation on Sterilizable Polymer Battery Separators, *E. F. Cuddihy and J. Moacanin*

1. Introduction

Sterilizable battery separators have been prepared from a graft copolymer of poly(potassium acrylate) and polyethylene. This and two preceding articles (SPS 37-50, Vol. III, pp. 166–169, and 37-52, Vol. III, pp. 98–100) report on the continuing efforts to characterize these materials by investigating their chemical and physical properties.

2. Irreversible Dehydration

After service as a separator in Ag–Zn batteries, the initially supple and very elastic membranes are found upon removal to have become brittle, fragile, and easily susceptible to cracking or tearing. Also, these materials become devoid of absorbed water and fail to absorb water from the atmosphere. This is in contrast with the virgin membrane material which equilibriates rapidly in air and at room temperature with large quantities of water (Fig. 5). Further, the elasticity and suppleness of the initial membranes were related to their water content, becoming increasingly brittle as the water content decreased. However, upon exposure to the ambient atmosphere, the virgin membranes quickly resorbed moisture and again became supple and elastic. The loss of hygroscopic properties after battery service was labeled "irreversible dehydration."

The explanation is simple, though it was attendant with a surprising result. The membrane is prepared by grafting chains of poly(potassium acrylate), PKA, on a film of polyethylene (PE). The PE is 50% crystalline and, after grafting, the crystalline content remained unchanged, indicating that all of the grafted PKA was present in the amorphous phase of the PE. The glass transition temperature T_g of PKA is above room temperature, and therefore this material should be hard at ambient conditions. Thus, the incorporation of PKA should render the film brittle. But absorbed water plasticizes the PKA, lowers its T_g below room temperature, making PKA rubbery, and hence the film becomes supple. Thus, the water content directly controls the elastic to brittle property range of the film by its plasticizing action in raising or lowering the T_g of PKA.

In turn, it is a property of the potassium cation to retain in the film sufficient water for plasticization. Reference to Fig. 6, which is reproduced from the literature (Ref. 1), details the influence of the cation on the ability of acrylate–ethylene systems to retain water. Starting with potassium, the propensity for retaining water decreases through sodium, to lithium, and finally to divalent cations, which give almost totally non-hygroscopic properties to the film. Thus, a film prepared with a divalent cation would be brittle at all times in air at room temperature.

Membranes during battery service are exposed to an electrolyte rich in zinc oxide, and it was reasoned that cation exchange between potassium and zinc could occur. This divalent cation would render the film non-hygroscopic and "irreversible dehydration" would result. Analyses for cation identification and concentration were carried out on samples of battery separators both before and after battery service, and the results are given in

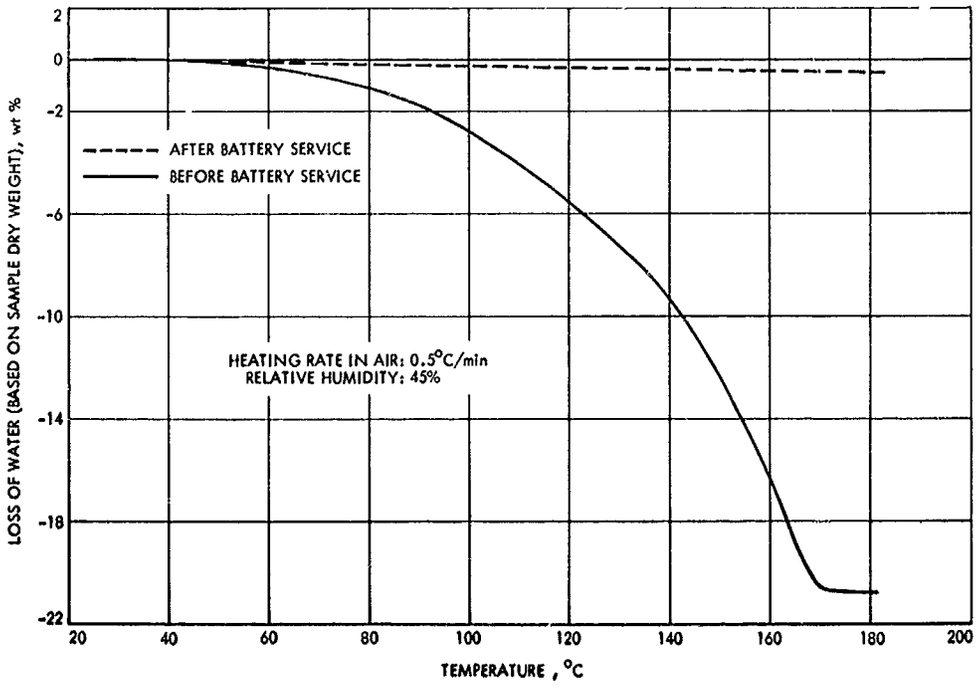

Fig. 5. Thermogravimetric analysis of GX-119 battery separator membranes

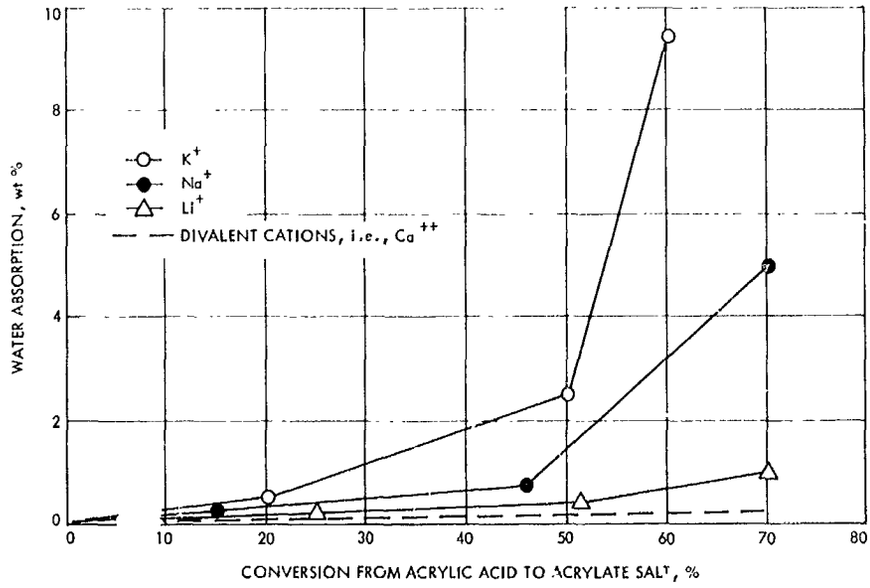

Fig. 6. Retained water content of a 14.8% acrylic acid–85.2% ethylene copolymer after 24-h water immersion at room temperature

Table 1. Expectantly, the separator before service contained dominantly potassium, but the membrane after service contained, quite unexpectedly, not the divalent cation zinc, but the divalent cation calcium. Although the presence of calcium explains why the membranes after battery service are non-hygroscopic, the origin of the calcium is as yet unexplained.

Table 1. Principal cations and their concentrations in GX-119 battery separator membranes before and after battery service

Cation[a]	Sample,[b] wt %	Concentration,[a] meq/g
Before battery service[c]		
K	8.20	2.09
Ca	0.44	0.22
Na	0.23	0.10
Mg	0.14	0.11
Ag	0.005	—
After battery service[d]		
Ca	4.10	2.06
Zn	0.74	0.22
Mg	0.67	0.55
K	0.47	0.12
Ag	0.008	—

[a]Identification and concentration obtained by spectroscopic analysis of the membranes.

[b]Wt. % calculated by employing dry weight of membrane sample.

[c]As received from Southwest Research Institute.

[d]Sections of battery membrane material after service contain a deposit of a blackish substance, presumably Ag_2O. For this study, care was taken to ensure that these sections were eliminated prior to the analysis.

Soaking the poly(calcium acrylate)-containing membranes in mild acid and then in aqueous KOH exchanges potassium for calcium, and the membranes regain their initial suppleness.

3. Zincate

A further point related to the cation exchange is concerned with the state of zinc oxide when dissolved in 40% KOH-H_2O solution. It is currently accepted that zinc oxide reacts with hydroxide to yield the zincate anion $ZnO_2^=$, and hence there would be no free zinc ion in solution to exchange with the potassium. This was subsequently tested by placing a piece of membrane containing PKA in a solution of ZnO in distilled and deionized water and another in a 40% KOH–H_2O solution saturated with zinc oxide. Cation exchange to zinc only occurred in the membrane placed in the zinc-oxide water solution, where zinc ions are known to exist. No zinc exchange occurred from exposure in the alkaline solution, indicating the absence of any free zinc ions.

4. Simple Analytical Technique for Acrylate Content

The battery separator membrane assumes non-hygroscopic properties not only in the presence of divalent cations but also when the acrylic part is in the acid state.

Hence, very accurate weighings of the membranes in either state can be made in air without interference from atmospheric moisture. Thus, the difference in weight of a sample when in the acid form and when containing a divalent cation is directly related to the acrylate content. Complete conversion from acid to salt and vice versa can be accomplished usually within an hour by soaking the membranes in either a 5–10% acid solution or a basic solution of the hydroxide or oxide of the desired divalent cation. Confirmation of the complete conversion from one form to the other is easily obtained by the change in the very sensitive and strong IR peaks for the acid at 5.58 μ and the salt at 6.45 μ.

5. Crosslinking

The membranes are prepared by first grafting chains of PKA onto PE and then crosslinking the system with divinylbenzene (DVB). Both reactions are initiated by exposure to γ-radiation from a cobalt 60 source and occur exclusively in the amorphous phase of the PE. The crosslinking is required to ensure that the film stays together when heated during sterilization at temperatures above the PE melting point of 107°C.

The extent of crosslinking can be obtained by measuring the stress–strain curves of the film when swollen in α-chloronaphthalene at 125°C. The high temperature is required to ensure that all the crystalline PE is melted and will therefore give no contribution to the mechanical strength. In addition, the swelling in a good PE solvent is required to disentangle the polymer chains and cause them to separate only to the extent allowed by the crosslinks. Hence, the strength of the film as measured by the initial modulus of the stress–strain curves will now be directly related to the number of crosslink sites.

Stress–strain measurements at 125°C in α-chloronaphthalene were carried out on (1) a membrane both grafted and crosslinked, (2) a membrane just grafted, and (3) a membrane just crosslinked. The results, summarized in Table 2, show that the grafted and crosslinked sample has a crosslink density of 1120×10^{-6} moles crosslink chains/cm^3, the just-grafted sample has a crosslink density of 669×10^{-6} moles crosslink chains/cm^3, while the sample presumably crosslinked with DVB, the crosslinker, was so negligibly crosslinked it couldn't be measured. For comparison, crosslinked rubbers typically have values between $100–200 \times 10^{-6}$ moles crosslink chains/cm^3 while hard, cured epoxy resins have values in excess of 1120×10^{-6}.

The surprisingly high value of 669×10^{-6} for the just-grafted membrane clearly indicates that the grafted chains

Table 2. Mechanical properties at break[a] and crosslinking densities of battery separator membranes for the GX-119 series

Membrane description	Tensile strength, psi	Elongation, %	Crosslink density,[b] moles crosslink chains/cm^3
Both grafted with poly(potassium acrylate) and crosslinked with divinyl benzene	540	29	1120×10^{-6}
Just grafted with poly(potassium acrylate)	445	40	669×10^{-6}
Just crosslinked with divinyl benzene	← Footnote c →		

[a]Stress–strain measurements obtained at 125°C on samples swollen in α-chloronaphthalene. This permits the direct measurement of the contribution to properties from the crosslinked network, and therefore the crosslinking density.

[b]For comparison, rubber has a crosslink density between 100 to 200 moles crosslink chains/cm^3.

[c]Stress–strain measurements unobtainable since sample came apart in α-chloronaphthalene at 125°C.

are actually crosslinking the system. Given now the concentration of these chains in the membrane, as well as the amount of PKA in the film, the molecular weight of the PKA chain is readily calculated to be 780, which corresponds to a degree of polymerization of 7.

After grafting, DVB is then incorporated into the film, and the crosslink density increases from 669×10^{-6} to 1120×10^{-6}. Clearly, if this difference of $(1120 - 669) \times 10^{-6} = 451 \times 10^{-6}$ existed in the PE film just crosslinked with DVB, it would have had a reasonable strength, but, in actual fact, it disintegrated in α-chloronaphthalene. Since the amounts of reacted DVB are equal in both cases, the implication is that more of the DVB is consumed in a crosslinking capacity in the presence of acrylate than is in the presence of PE only. Perhaps, in absence of PKA, DVB tends to polymerize into long chains of poly(divinylbenzene) rather than induce crosslinking.

In the early stages of development of these membranes at Southwest Research Institute, the procedure was to crosslink first, followed by grafting. However, inferior products were obtained. Subsequently, the procedure was reversed and greatly improved membrane materials were obtained. Perhaps, as the results here indicate, the crosslinking densities in their initial products were too low, or the DVB in the PE interfered with PKA grafting.

One final point on crosslinking is worth noting. As has been pointed out, the membranes during battery service are experiencing cation exchange from potassium to calcium. This divalent cation, by connecting across two acrylate groups, increases the crosslinking density. If, during battery service, degradative reactions are occurring which destroy the crosslinking introduced by the PKA and DVB, then the cation exchange to calcium would provide offsetting crosslinking and preserve the mechanical strength of the membrane. Some evidence of this was obtained by converting a used battery separator from the calcium salt back to the potassium salt, and noting that, although the elastic and supple properties returned, the material had greatly reduced tear resistance as compared to a membrane that had not seen battery service.

c. Silver Oxide Problem

During battery operation, silver oxide (Ag_2O) is formed on the silver electrode, and this material has a finite solubility (4×10^{-1} molar) in the KOH–H_2O electrolyte. Silver oxide can then freely migrate to the zinc electrode, where it can be reduced to metallic silver. The membrane's intended function, in dividing the cell, is to keep the dissolved silver oxide on the silver electrode's side. However, some silver oxide does permeate the membrane, but also there is a continuous deposition of solid silver oxide within the interior of the membrane. This deposition continues until the volume concentration of the silver oxide builds to a sufficient level where battery performance deteriorates due to the onset of "high-resistant–short-circuiting" across the membrane. Even an insulating solid in thin enough layers can have some measurable electrical conductivity.

This deposition is a failure mode of the battery, as are any problems which arise from metallic silver accumulation at the zinc electrode. In addition, silver oxide dissolved in strong alkaline medium is a strong oxidizing agent, intermediate between the oxidizing powers of permanganate and perchlorate. This can lead to oxidative damage of the membrane, such as oxidative scission of the crosslinking introduced by the PKA and DVB reactions. Perhaps this is the testimony to the desirability of the divalent cation exchange in the membrane to preserve the crosslinking level. Finally, another failure mode, unrelated to silver oxide, is the growth at the zinc electrode of crystalline whiskers whose sharp points can pierce the membrane and provide a direct short-circuit path, which may eventually touch th silver electrode.

Although there is considerable effort being expended to find solutions for each of the failure modes posed by the presence of the dissolved silver oxide, such as permselective membranes, one direct approach seems to lie in finding methods to simply reduce silver-oxide solubility —additives, for instance, which would not interfere with battery operation but which would lower or eliminate silver-oxide solubility. The feasibility of this approach was demonstrated by observing that the solubility of silver oxide was reduced by a factor of over 20 in a solution of 40% KOH in a mixed solvent system of 80 vol % water and 20 vol % methanol. Though this solution is compatible with the membrane, it performed poorly as a battery electrolyte, as can be seen from its current–voltage characteristic curve given in Fig. 7. In fact, all solutions containing greater than 5 vol % methanol failed as candidate electrolytes, all giving gaseous products at the negative electrode at an applied potential of only 0.6 V. The Ag–Zn batteries are normally changed at an applied potential of 1.5 to 1.6 V.

Investigations will continue on electrolyte systems which are operational in a Ag–Zn battery and which will have lowered silver-oxide solubility.

Reference

1. Bonotto, S., and Bonner, E. F., *Polymer Preprints*, ACS, Vol. 9, No. 1, p. 537, Apr. 1968.

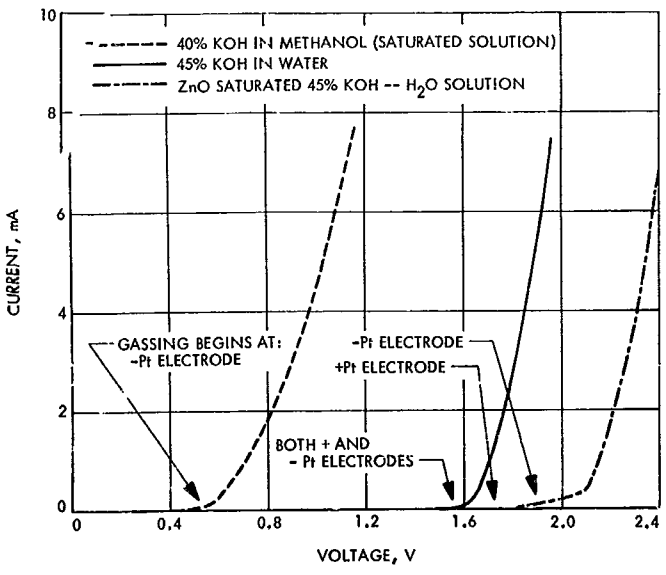

Fig. 7. Current–voltage characteristic curves for various battery electrolytes measured by employing platinum electrodes

C. Creep of Elastomer Undergoing Aging,

J. Moacanin, H. Y. Tom, R. F. Fedors, and R. F. Landel

1. Introduction

A long-standing goal of the research program on the mechanical properties of solid composite propellants and their elastomeric binders has been to be able to predict their properties from molecular parameters characteristic of the binders (Refs. 1 and 2). This goal has now been reached and a comprehensive theory developed (Ref. 3).

For example, modulus values, as well as breaking strengths, can be estimated over wide ranges in time or temperature without using any arbitrary parameters. Though developed in a program related to solid composite propellants, these results also have implications for long time behavior of materials such as sealants for high-speed aircraft fuel tanks, or rubbers for shock mounts. However, in the long time region, i.e., at quasi-equilibrium in terms of the kinetic theory of rubberlike elasticity, there are two main reasons that prevent a straightforward application of this development: (1) the theory in its present form does not account for degradation reactions, which may be too slow to be ascertained from short time measurements; (2) there exist poorly understood slow relaxation processes whose effects are presently accounted for by an empirical equation due to Plazek (Ref. 4).

Plazek studied the creep compliance in shear of natural rubber and styrene-butadiene rubber (SBR), but also found that Thirion's (Ref. 5) stress relaxation data on specimens from the same sheets were in complete accord with his creep data. (Both were very careful to exclude chemical degradation.) The good agreement between the results from these two types of experiments and our own constant strain-rate data confirm the validity of Plazek's equation but, of course, this does not mean that it will be generally valid for all elastomers.

Therefore, a program has been initiated to combine our studies on mechanical properties with those on the chemical reactions of such materials to develop, through an interdisciplinary approach, improved methods of predicting long-term or fatigue behavior of such materials. This article explores in particular the implications of Plazek's work on the interpretation of the creep behavior of slowly degrading systems.

2. Discussion

Plazek showed that, in addition to the usual time–temperature superposition for the viscoelastic response of a crosslinked elastomer, a superposed curve for long time response could be obtained using the apparent molecular weight between crosslinks M_c as a reduction variable. Thus, by carrying out measurements at several temperatures and M_c levels, one can obtain the viscoelastic response for a reference temperature and reference M_c over 9 or 10 decades of logarithmic time.

Plazek's master curve for creep compliance—the starting point for this work—is shown in Fig. 8 and is given by

$$\log J_x\left(\frac{t}{a_x}\right) = \log J_e(M_c) + \log\left[\frac{J_e(M_{ref})}{J_e(M_c)}\right] + \log \psi_x\left(\frac{t}{a_x}\right) \quad (1)$$

where $J_e(M_c)$ is the equilibrium compliance corresponding to M_c, the ratio in the second term represents the vertical shift that brings the response for the specimen onto the level of the reference curve, and ψ is a terminal retardation function which describes the very slow approach to equilibrium. The factor $\log a_x$, which provides the reduced

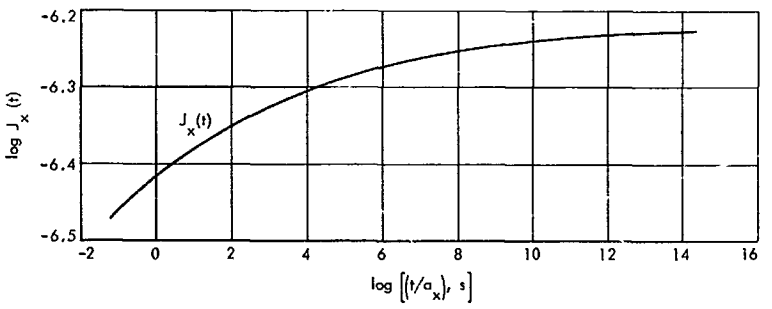

Fig. 8. Logarithmic plot of $J_x(t)$, extended compliance curve resulting from reduction using M_c as a reduction variable, vs logarithm of reduced time t/a_x (M_c varies between 5200 and 20,500)

time scale, represents the horizontal shift necessary to achieve superposition. The shift factor a_x was found to be an exponential function of M_c:

$$a_x = \text{const} \times M_c^m \tag{2}$$

with $m = 15.4$ for both natural rubber and SBR.

It follows from this development, once the master curve for an elastomer is established and, consequently, the $a_x - M_c$ relationship is known, that M_c is the only parameter needed to predict the creep compliance of a given specimen at time t. Also, one can use the compliance curve to calculate other rheological properties via the distribution of retardation times.

Accepting that the above considerations account for mechanical effects, the relationship between a_x and M_c suggests a method of incorporating the effects of chemical changes into the same formalism. We merely let M_c, and hence a_x, become a time-dependent parameter whose value is determined by the appropriate degradation kinetics.

For studying degradation, it is preferable to use the effective number of chains ν_e as the operational parameter, instead of M_c. The relationship between the two is taken as $\nu_e = \rho/M_c$ moles/cm³. Note that M_c, the apparent molecular weight of a network chain as defined here, is not the same as M_c', the true molecular weight of an elastically effective chain; in general, $M_c > M_c'$.

For the description of a system undergoing degradation, it is appropriate to use the initial material as reference; then the master curve describes the behavior of the undegraded material. As degradation proceeds, a_x departs from unity:

$$a_x(t) = \left[\frac{M_c(t)}{M_c(0)}\right]^m = \left[\frac{\nu_e(0)}{\nu_e(t)}\right]^m \tag{3}$$

By an appropriate horizontal shift, i.e., log $a_x(t)$, and vertical shift, i.e., log $J_e(0)/J_e(t)$, in a double logarithmic plot of $J(t)$ versus t, one arrives at the compliance of the degraded material. This statement implies that the state of the system is determined uniquely by the value of $a_x(t)$, and does not depend on its history. This is an approximation whose effect is illustrated in Fig. 9. The two solid curves indicate the compliance–time relationships for elastomers, in the absence of degradation, cross-linked to different extents.

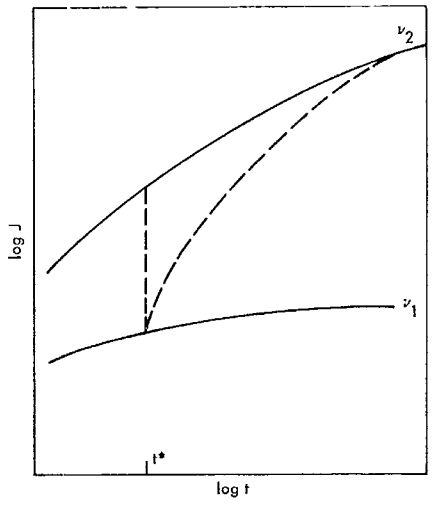

Fig. 9. Implication of the assumption that the network responds instantaneously to changes in ν_e

Now suppose that specimen ν_1 is suddenly degraded to ν_2 at t^*. According to this approximation, it should assume instantaneously the compliance for ν_2 at t^*. Clearly, this is an idealized situation, for a real system would gradually approach the curve ν_2. The approximation should not be too serious, however, as long as the degradation processes are slow, because then $\nu(t + \Delta t)/\nu(t) \approx 1$, i.e., the two curves are close together, and the difference in the paths is very small. Moreover, the approximation overestimates the rate of creep, and, therefore, will lead, for example, to conservative fatigue estimates.

It is to be noted that considerable work has been done on the behavior of elastomers at elevated temperatures (Ref. 6). Under these conditions, ψ_x may approach unity. If so, it can be assumed that the elastomer is at equilibrium (i.e., at J_e) at all times, and, hence, relating changes in the mechanical response to degradation is straightforward.

Initially, there are $\nu(0)$ chains. At time t we suppose that $q(t)$ cuts have occurred, some of which may be multiple cuts on the same chain, leaving $\nu(t)$ elastically effective chains to support the load. These are the chains which have not experienced a single cut. It is necessary, therefore, to derive the relationship between $\nu(t)$ and $q(t)$, i.e., $\nu[q(t)]$, since the mechanical response is determined by $\nu(t)$ whereas chemical kinetics of degradation will yield $q(t)$.

As an illustration of the approach to be taken in incorporating degradation kinetics, let's consider the simple

case of first-order kinetics which has been shown to apply to some real systems, e.g., oxidative degradation of natural rubber. If each cut were effective, then

$$\nu(t) = \nu(0) - q$$

and, in accordance with the postulated kinetics,

$$\frac{d\nu(t)}{dt} = -k'\nu(t)$$

or

$$\frac{\nu(t)}{\nu(0)} = \exp(-k't)$$

Also, in view of Eq. (3),

$$a_J(t) = \exp(mk't) \qquad (4)$$

Figure 10 shows the compliance curve for an elastomer where M_c is 20,500, m is 15.4 (the value for natural rubber), and where $\nu(t)/\nu(0) = \frac{1}{2}$ after 1 day in one case, and after 1 yr in the other case. It is apparent that, after one half-life, properties deteriorate too rapidly to be of much interest.

Future work will use existing kinetic data for a system like natural rubber to estimate the degradation rate at low temperatures, such as ambient, and then attempt a realistic comparison of the predicted and experimentally determined behavior. Such an analysis is necessary to ascertain the range of conditions where one may expect to be able to separate chemical from purely mechanical contributions to behavior.

References

1. Landel, R. F., and Fedors, R. F., *Processes in Polymeric Solids*, p. 361. Interscience Publishers, New York, 1964.
2. Landel, R. F., *Office of Naval Research Structural Mechanics Series, Mechanics and Chemistry of Solid Propellants*, proceedings of the Fourth Symposium on Naval Structural Mechanics, pp. 575. Pergamon Press, New York, 1967.
3. Fedors, R. F., and Landel, R. F., "A Test of the Predictability of the Properties of Filled Systems," presented at the AIAA Meeting, Washington, D.C., June 1967.
4. Plazek, D. J., *J. Poly. Sci.*, A-2, Vol. 4, p. 745, 1966.
5. Thirion, P., *Proceedings of the International Conference on the Physics of Non-Crystalline Solids*, p. 345. North Holland, Amsterdam, 1965.
6. Tobolsky, A. V., *Properties and Structure of Polymers*, Chapt. V. John Wiley & Sons, Inc., New York, 1960.

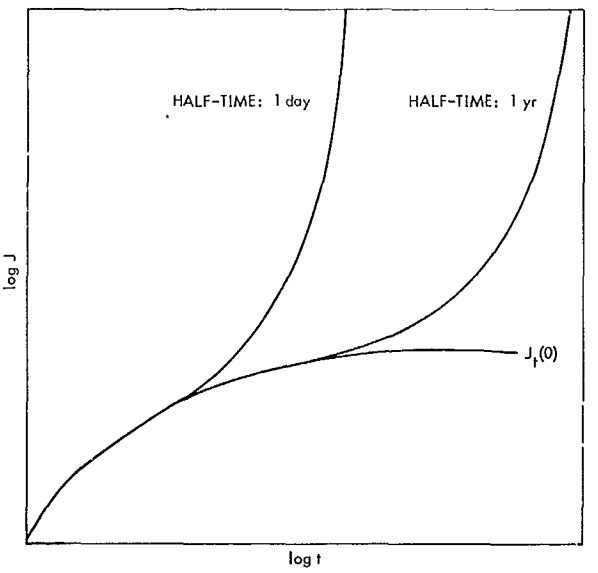

Fig. 10. Compliance curves for networks undergoing degradation

D. Stress Relaxation in Compression of SBR–Glass Bead Composites,

J. Moacanin and H. Y. Tom

1. Introduction

A solid-propellant grain undergoing heat sterilization experiences a complex history of tensile and compressive stresses. A simple test was devised to ascertain the changes which may be taking place in the propellant during sterilization. A cylindrical polyurethane propellant slug was confined to a fixed length in the clamp; the ends of the specimen were bonded to the clamp plates. Starting at room temperature, the specimen was unstressed. As the temperature was gradually raised to 135°C, the specimen experienced compressive stresses (Fig. 11) because its expansion was restricted. While the temperature was maintained at 135°C, stress relaxation took place; the final stress level was about ¼ of its maximum value. At the end of the cycle, when the specimen was cooled to room temperature, it experienced a significant tensile stress. The specimen did not return to its initial unstressed state, because the relaxation at 135°C was caused in part by chemical exchange of the urethane bonds in the binder. At room temperature, however, the rate for this process is too slow to contribute to the overall relaxation process.

These observations could not be interpreted quantitatively, however, because stress relaxation is caused by

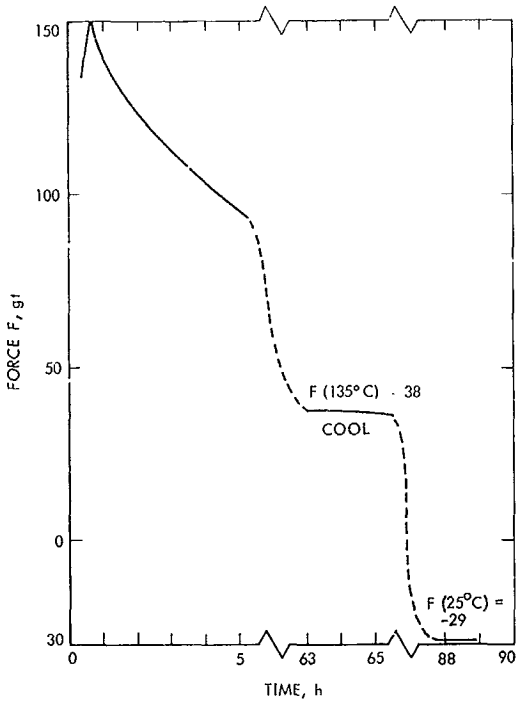

Fig. 11. Stress in a polyurethane propellant test specimen undergoing heat sterilization

the superposition of the following effects: mechanical relaxation, dewetting of filler, and chemical degradation and exchange reactions. To identify and ultimately assess the extent of each contribution, a separate study was conducted on the stress relaxation in compression of styrene–butadiene rubber (SBR) filled with glass beads. For the experimental conditions which were used, chemical degradation and exchange reactions should be negligible. Thus, these experiments enabled us to focus our attention on the contribution of dewetting.

2. Experimental Technique

Styrene–butadiene rubber test specimens loaded with varying amounts of glass (0.000 to 0.339 volume fraction) were prepared, following a slightly modified procedure described previously for thin sheets (SPS 37-32, Vol. IV, pp. 120–125). The test specimens (1.2 cm long × 1.8 cm diameter) were cured in the press for 3 h at 154.5°C, and then let stand in a vacuum chamber for 3 h at 130°C, before removal from the mold. By including the last step, clear bubble-free specimens could be obtained. The effective number of chains ν_e was assumed to be the same for all samples, since the same peroxide concentration was used; determinations of their values by swelling are underway.

The stress relaxometer was constructed with a LVDT load cell (Daytronic, 152A), excited and amplified by a signal conditioner (Daytronic, 300 D with type 71 plug-in module). The output from the force transducer was recorded by a strip chart recorder (Leeds and Northrop, model G). To minimize temperature fluctuations in the load cell, a flow of nitrogen gas maintained at room temperature was circulated past the head. A further precaution against thermal influence was taken by extending the coupling between the head and sample with a long univar rod. The stability of this instrument over a 24-h period was found to be ±20 g.

In a typical experiment, the test specimen was placed between two plates, where one was fixed and the other coupled to the load cell. The sandwiched specimen was then immersed into an oil bath fixed at 50 ±0.5°C. After ½ h, it was gradually compressed until a reasonably high stress was attained. The gage reading corresponding to the initial length l_0 was determined by extrapolating linearly to zero force. The specimen was then allowed to relax at l_0 for at least 10 min before compressing to the desired level.

The stability of the experimental setup was assessed by conducting a control experiment for 24 h with the test specimen held at l_0. No increase in instrument instability or significant oil sorption from the constant temperature were observed.

The following changes would substantially improve the instrumentation. Better temperature control for the electronics would minimize drift and therefore improve long time stability. A clamp to quickly strain the test specimen (< 1 s versus 15–20 s required now) would extend data to short times.

3. Results and Discussion

In earlier articles,[2] various aspects of the mechanical behavior of composite systems in tensile deformation have been discussed in some detail. In particular, strain-induced particle-binder dewetting was described, and a theoretical model was proposed which predicts the isothermal volume dilatation. Pursuant to these investigations, the reinforcing effect of the filler particle is proportional to the loading fraction ϕ and the fraction of the filler surface in contact with the binder. Thus, for

[2]SPS 37-32, Vol. IV, pp. 120–125; SPS 37-35, Vol. IV, pp. 93–98; SPS 37-40, Vol. IV, pp. 80–83; and SPS 37-41, Vol. IV, pp. 97–107.

small strains without dewetting, the modulus E for the filled system is related to that of the binder E_0 by

$$\frac{E}{E_0} = \left(1 - \frac{\phi}{\phi_m}\right)^{-2.5} \tag{1}$$

where ϕ_m is the maximum attainable volumetric loading fraction.

As the binder pulls away from the filler surface, the effective loading level for tensile deformation and a spherical filler particle is given by

$$\phi_{eff} = \phi \sin\theta \tag{2}$$

where the angle $\theta = 90$ deg $- \theta$ defined in SPS 37-41, Vol. IV.

This result was obtained by assuming that the void formed is conical in shape. The fraction of particle surface still in contact with the binder is then given by $S_a = \sin\theta$, where the angle θ defines the base of the tensile cone in contact with the sphere (Fig. 12). Using the same model for compression, instead of two cones with their axis parallel to the direction of stress, one obtains a doughnut-shaped body with the axis of revolution parallel to the compressive stress. Carrying out the analysis, we arrive at $S_a = \sin\theta$, leading to

$$\phi_{eff} = \phi\,(1 - \sin\theta) \tag{3}$$

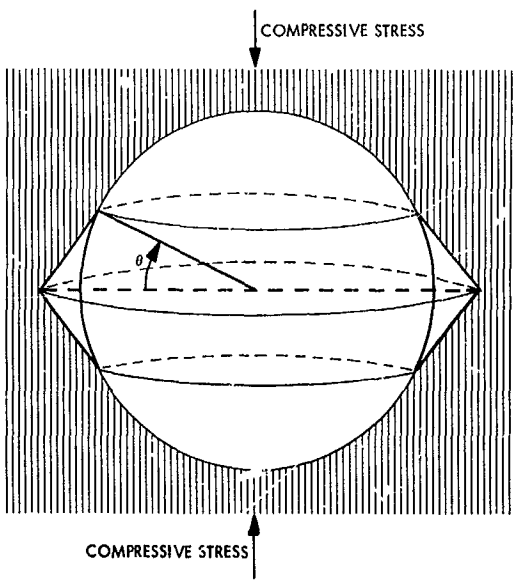

Fig. 12. Schematic of dewetting

Allowing ϕ_{eff} to vary with time, because of dewetting, Eq. (1) can be rewritten as

$$\frac{E}{E_0} = \left(1 - \frac{\phi_{eff}}{\phi_m}\right)^{-2.5} = \left(1 - \frac{\phi}{\phi_m}\right)^{-2.5} \left(1 + \frac{\frac{\xi_t}{\phi_m}}{\frac{1-\phi}{\phi_m}}\right)^{-2.5} \tag{4}$$

where

$$\phi_{eff}(t) \equiv \phi - \xi_t$$

ϕ being the value for $t = 0$; hence, ξ_t represents the decrease in ϕ for given t. Since by postulate ϕ_{eff} is proportional to S_a, then

$$\frac{\phi_{eff}(t)}{\phi} = 1 - \sin\phi = 1 - \frac{\xi_t}{\phi}$$

or

$$\sin\theta = \frac{\xi_t}{\phi}$$

On the other hand, it was found (SPS 37-41, Vol. IV) that the rate of volume dilation in tension is proportional to the cube root of time $t^{1/3}$. Accepting the same relationship for compression, one can write

$$\frac{\Delta V}{V_0} = \frac{\phi}{2}\frac{\sin^3\theta}{1 - \sin^2\theta} = \frac{\phi}{2}\left(\frac{\frac{\xi_t^3}{\phi^3}}{1 - \frac{\xi_t^2}{\phi^2}}\right) = \beta t^{1/3}$$

Thus

$$\beta^{1/3} t^{1/9} = \frac{\left(\frac{\phi}{2}\right)^{1/3}\frac{\xi_t}{\phi}}{\left(1 - \frac{\xi_t^2}{\phi^2}\right)^{1/3}} = \left(\frac{\phi}{2}\right)^{1/3}\frac{\xi_t}{\phi} + 0\left(\frac{\xi_t^3}{\phi^3}\right)^{1/3} \tag{5}$$

Only the term in ξ_t/ϕ need be retained, since the ratio is $\ll 1$. With the proper substitutions, Eq. (4) predicts for compression

$$\frac{\sigma}{\sigma_0} = \left(1 - \frac{\phi}{\phi_m}\right)^{-2.5}\left[1 + \frac{\frac{\phi}{\phi_m}}{\frac{1-\phi}{\phi_m}}\left(\frac{2\beta}{\phi}\right)^{1/3} t^{1/9}\right]^{-2.5} \tag{6}$$

or

$$\left(\frac{\sigma_0}{\sigma}\right)^{0.4} = \left(1 - \frac{\phi}{\phi_m}\right) + \frac{\phi}{\phi_m}\left(\frac{2\beta}{\phi}\right)^{1/3} t^{1/9} \qquad (7)$$

From Eq. (7), it follows that a plot of $\sigma_0/(\sigma)^{0.4}$ should be linear in $t^{1/9}$, the intercept giving $(1 - \phi/\phi_m)$ and the slope being $\phi/\phi_m(2\beta/\phi)^{1/3}$.

The experimental results for the SBR–glass beads system were treated according to the above scheme. Figures 13 and 14 show the data for 7% and 18% compression, respectively. For the 7% data, the scatter does not allow for a meaningful estimate of the slopes. The intercepts, however, are reasonably well defined. For the 18% data, both the intercepts and the slopes are better defined. The various parameters calculated from the analysis of these plots are given in Table 3.

Inspection of Table 1 shows that the estimates of ϕ from the plots are lower than the filler volume fractions. The deviations are illustrated in Fig. 15. The equation used to calculate the lines is

$$\phi_{eff} = \frac{\phi_0}{1 + k\epsilon\left(\frac{1}{1 - \phi_0^{1/3}}\right)} \qquad (8)$$

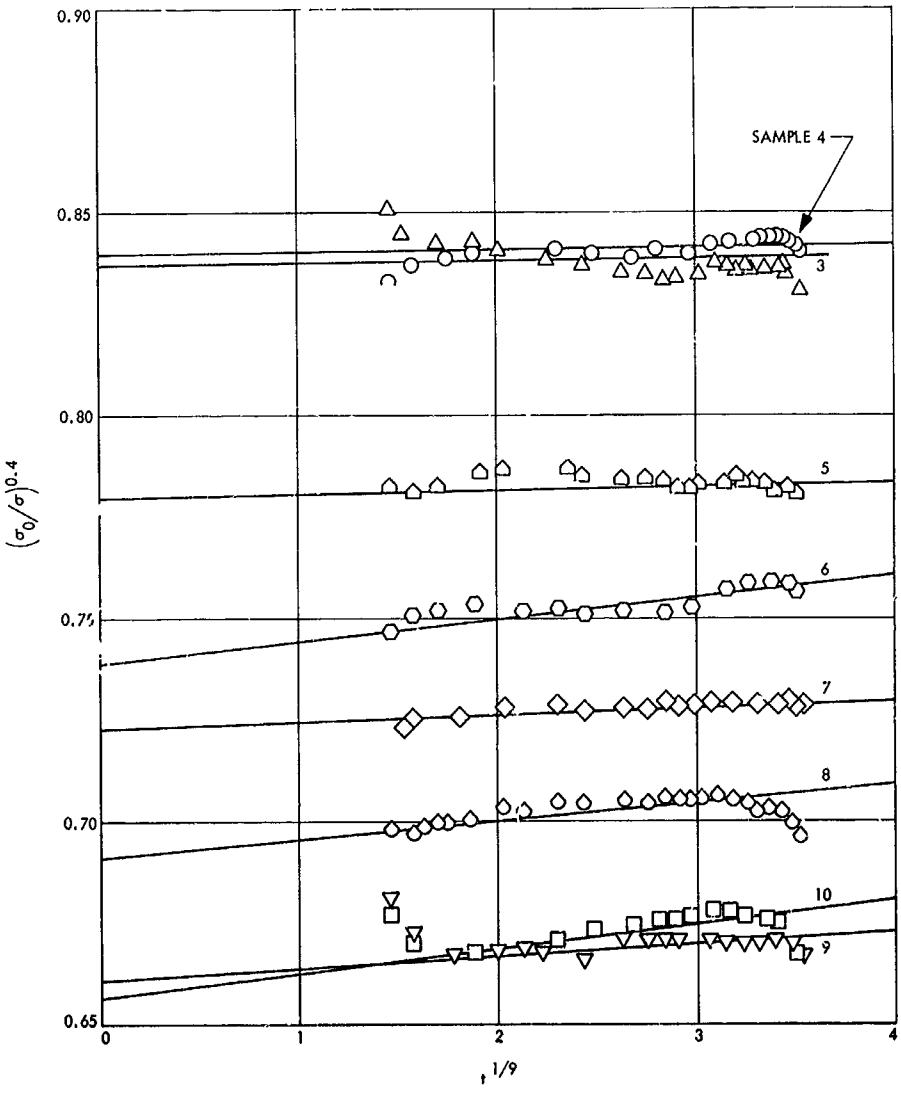

Fig. 13. $(\sigma_0/\sigma)^{0.4}$ vs $t^{1/9}$ for 7% compression

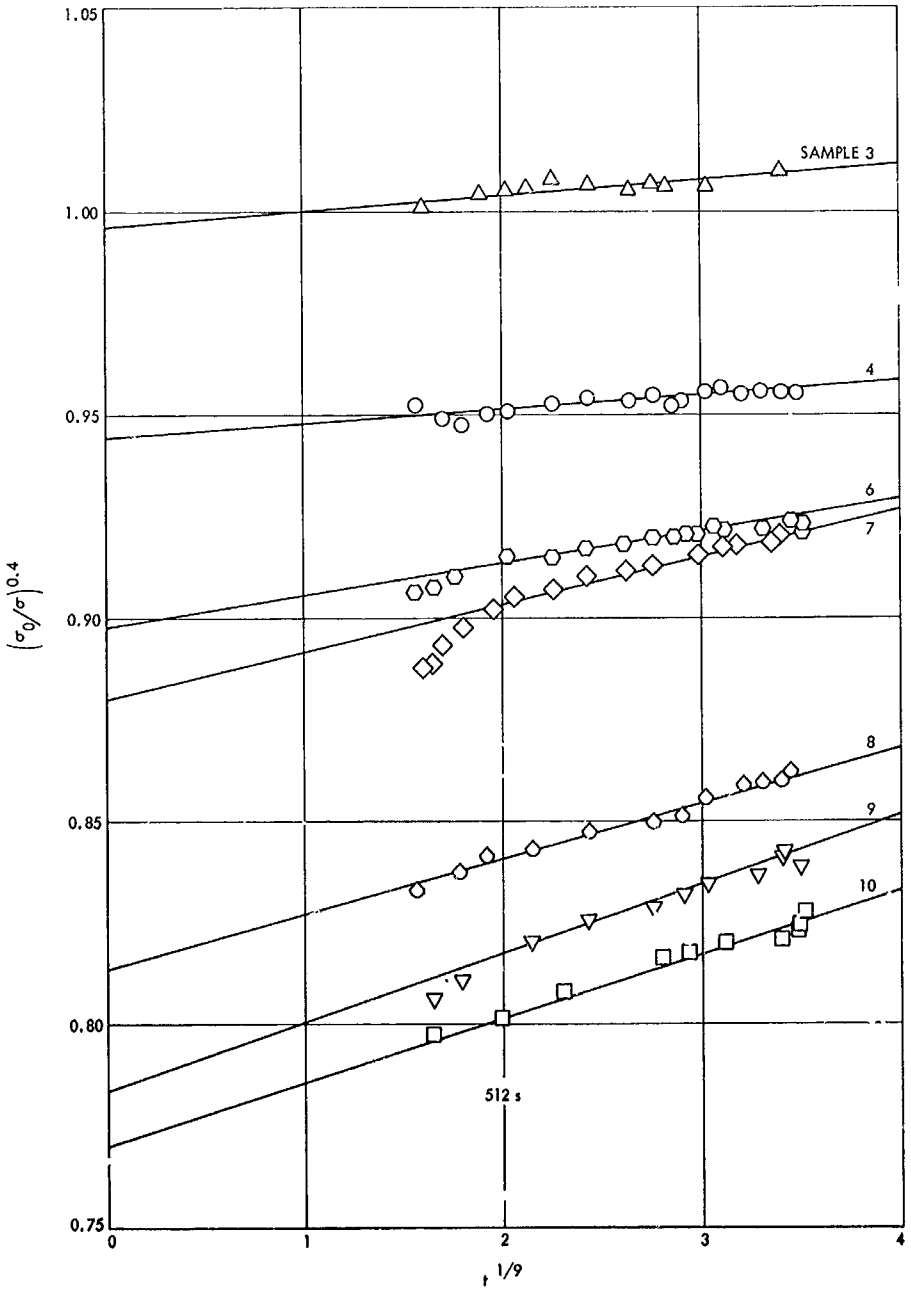

Fig. 14. $(\sigma_0/\sigma)^{0.4}$ vs $t^{1/9}$ for 18% compression

Table 3. Parameters from $(\sigma_0/\sigma)^{0.4}$ vs $t^{1/9}$ plots according to Eq. (7) for 7% and 18% compression

Sample number	Glass-bead volume fraction ϕ	$(1 - \phi/\phi_m)$		$\phi(\phi_m - 0.74)$		$\phi^{2/3}/\phi_m \times (2\beta)^{1/3}$		$(2\beta)^{1/3}$
		7%	18%	7%	18%	7%	18%	18%
3	0.092	(0.84)[a]	(0.97)[c]	0.045	0.02	—	0.004	0.22
4	0.132	0.84	0.954	0.12	0.034	0.004	0.0035	0.20
5	0.169	0.78	—	0.16	—	[b]	—	—
6	0.204	0.74	0.907	0.19	0.069	0.005	0.0066	0.055
7	0.234	0.724	0.879	0.21	0.09	0.002	0.0117	0.068
8	0.270	0.69	0.814	0.23	0.14	0.005	0.014	0.070
9	0.29	0.66(?)	0.779	0.25	0.16	0.003	0.017	0.080
10	0.35	0.66	0.756	0.25	0.18	0.012	0.016	0.072

[a]Used ϕ extrapolated.
[b]Bad plot.
[c]Plot gives ≈ 1.0, hence $\phi \approx 0$; 0.97 is lower limit of estimate of uncertainty.

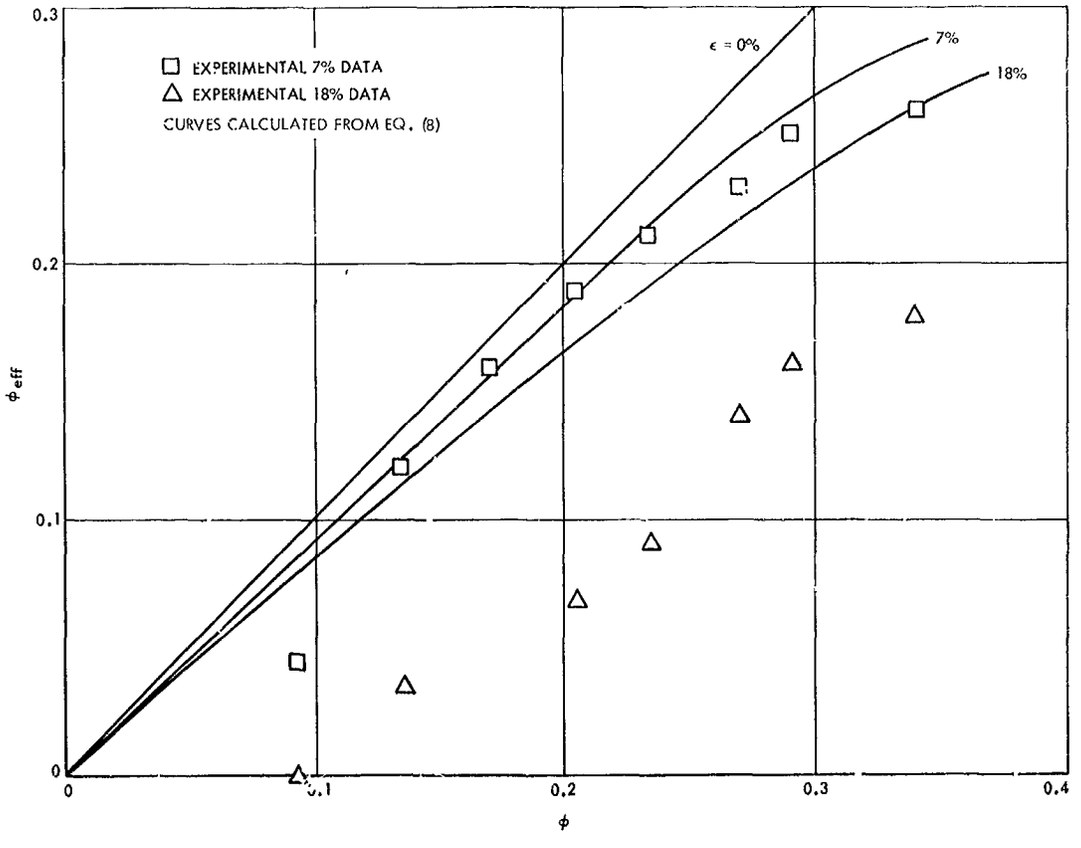

Fig. 15. Comparison of volumetric and effective filler fractions

where $k = 1/2$). Included in the equation is a correction for the fact that in a filled system the total strain is taken up by the binder alone, but does not include dewetting.

The data points in Fig. 15 are the estimates from the plots according to Eq. (7). For 7% compression, the agreement is good. For 18% compression, the points are much below the corresponding curve. This may be the consequence of partial instantaneous dewetting the moment the specimen is strained; thus, ϕ_{eff} corresponding to $t \to 0$ would be given by the extrapolation. Following this fast initial dewetting, the process then continues gradually at a rate proportional to $t^{1/9}$. This is in qualitative agreement with the previously reported volumetric

measurements, where for tensile deformation plots of $\Delta V/V_i$ versus $t^{1/2}$ were linear, with an intercept for $t = 0$ which was proportional to the strain.

The rate constant β for 18% compression was estimated from the data for the five highest loading levels to be about 0.2 (sec^{-1}). This value is in remarkable agreement with about 0.12 obtained from dilatrometric data for tensile deformation (SPS 37-41, Vol. IV). The fact that data from stress relaxation in compression lead to the same rate constant as those from volume measurements in tension strongly supports the basic correctness of the underlying model for dewetting. It also demonstrates that the contribution of dewetting to the mechanical behavior can be factored out.

XIII. Research and Advanced Concepts

PROPULSION DIVISION

A. Further Heat-Transfer Results With an Applied, Transverse Magnetic Field in a Square Channel, *E. J. Roschke*

1. Introduction

Some experimental heat-transfer results for partially ionized argon flowing in a 2- × 2-in. square channel with a transverse magnetic field were presented in SPS 37-51, Vol. III, pp. 130–135. Those results, and all results appearing in previous SPS publications, were for subsonic flow. The purpose of this article is to present some of the earlier data in a different way and compare it to the theory presented by Back.[1] Prominent in this treatment of both experiment and theory is the joule heating parameter S, which arises in the energy equation applicable to this problem. Methods of computing S are given; various methods for correcting S due to departures of the electrical conductivity from scalar values are discussed. In addition, new data for a case of supersonic flow is presented that is of interest because much higher values of S were obtained than in previous tests and much larger increases in heat transfer were measured than before. The apparatus and method of making experiments are described in SPS 37-51, Vol. III, and earlier articles in the SPS series. Symbols used in this article are defined in Table 1.

2. Method of Presenting Heat-Transfer Data

A convenient way of presenting the experimental heat-transfer data is in the form of the non-dimensional heat flux

$$Q^* = \frac{2aq}{k_i (T_i - T_w)} \tag{1}$$

This grouping tends to include the effect of changes in the bulk temperature of the gas that occur when the magnetic field is applied and then varied (see SPS 37-51, Vol. III). It is also one of the dependent variables utilized in the theoretical treatment (see Footnote 1). The effect of the applied magnetic field is emphasized by forming the ratio Q^*/Q_0^*, which represents the ratio of the non-dimensional heat flux with applied field to its value when the applied field is zero.

[1] Back, L. H., "Laminar Heat Transfer in Electrically Conducting Fluids Flowing Between Parallel Plates," paper accepted for publication in *Int. J. Heat Mass Transfer*.

Table 1. Nomenclature

a	channel half-height, $2a = 2$ in.
A, C	upper and lower walls of channel, respectively
B	applied magnetic field strength
c	specific heat
E	applied electric field strength
Ek	Eckert number, $Ek = \bar{u}^2/c\,(T_i - T_w)$
H	total enthalpy
Ha	Hartmann number, $Ha = (\sigma/\mu)^{1/2} Ba$
j	current density
K	ratio of applied to induced electric fields, $K = E/\bar{u}B = 0$
k	thermal conductivity (Ref. 2)
$\dot{m}$	mass rate of flow
Pr	Prandtl number (Ref. 2)
q	measured heat flux
Q^*	non-dimensional heat flux, $Q^* = 2aq/k_i\,(T_i - T_w)$
Q_0^*	non-dimensional heat flux at zero magnetic field
Re	Reynolds number based on channel height, $Re = \dot{m}/2a\mu$
S	joule-heating parameter, $S = (Ha)^2\,Ek\,(1 - K)^2\,Pr$
S'	corrected joule-heating parameter, $S' = S\,(1 + \beta_e\beta_i)$
T	temperature
$\bar{u}$	bulk gas velocity
x	axial coordinate in direction of flow
$\bar{x}$	non-dimensional axial distance, $\bar{x} = (x/2a)/RePr$
β_e	Hall parameter, $\beta_e = \omega_e \tau_e$
β_i	ion-slip parameter, $\beta_i = \omega_i \tau_i$
μ	viscosity (Ref. 2)
σ	scalar electrical conductivity (Ref. 2)
τ_e, τ_i	particle collision times
ω_e, ω_i	particle collision frequencies

Subscripts

i	inlet conditions
0	conditions at zero magnetic field
w	conditions at wall

In the theoretical treatment, k_i is constant because of the constant-property assumption and T_i may be considered fixed as Q^* changes with changing value of magnetic field B, i.e., changes in the joule heating parameter S. However, in the experimental case, both k_i and T_i vary with S at a selected inlet axial station. In practice, Q^* is calculated presently from

$$Q^* = \frac{2acq}{k_i\,(H_i - H_w)} \tag{2}$$

where c is an effective specific heat taken to be constant; H_i is obtained directly from an energy balance applied to the system in the axial direction. All semi-local bulk flow parameters (such as temperature, velocity, and ionization fraction) are obtained from the energy balance and iteration of the conservation equations; transport properties at the appropriate conditions are taken from Ref. 1. Presently, the inlet station is taken to be the center of the first segment of the four-segment test section (SPS 37-51, Vol. III), partly because the magnetic field distribution becomes approximately flat at that location. All heat-transfer data to be presented later, however, are for the second segment of the test section.

The variation of Q^*/Q_0^* with S at the selected axial station is then of interest for the channel walls perpendicular to the direction of the applied magnetic field.

3. Calculation of the Joule Heating Parameter

The joule heating term j^2/σ in the energy equation may be non-dimensionalized according to

$$S = (Ha)^2\,Ek\,(1 - K)^2\,Pr \tag{3}$$

Thus, the sign of S is always positive for a horizontal channel whether the direction of B is vertically upward or downward. The calculation of S from Eq. (3) is straightforward when all the bulk properties of the gas are known as a function of axial position. Since there is no applied electric field in the present experiments, $K = 0$.

However, at the considerably high values of applied magnetic field employed here (up to 10,000 G), departures of S from the value expressed by Eq. (3) are to be expected when the electrical conductivity departs from its classic scalar value. One correction commonly used is due to the Hall effect and S then becomes reduced in accordance with

$$S' = \frac{S}{(1 + \beta_e^2)} \tag{4}$$

In these experiments $\beta_e >> 1$ so that $S' \to 0$; theoretically, no effects of magnetic field on heat transfer would be observed. Since substantial changes in q and Q^* were obtained for negligible S' from Eq. (4), it is concluded that Eq. (4) cannot apply in the present experiments.

Hall and ion-slip effects were discussed in SPS 37-52, Vol. III, pp. 109–112. Those results indicated that $\beta_i \leq 10^{-2}\beta_e$ for argon and that the correction factor due to ion-slip alone would be zero when the Hall effect was zero ($\beta_e = 0$). The ion-slip effect, however, is not necessarily zero when the Hall effect is zero if the ions are current carriers (Ref. 2). Those results applied to the present situation yield a corrected value of

$$S' = \frac{S}{(1 + \beta_e\beta_i)} \tag{5}$$

which applies when the Hall current is zero and the component of magnetic field in the flow direction is small compared to the transverse component. The correction factor $(1 + \beta_e\beta_i)$ was successfully used to correlate experimental measurements for argon (Ref. 2) for conditions that may be similar to those in the present experiments.

4. Results for a Case of Subsonic Gas Flow

The results given in SPS 37-51, Vol. III, were obtained by manual calculation; since that time more refined calculations have been performed and many have been reduced to machine computation. The results for tests 107-18H and -19H (taken for the same flow conditions and applied electric power to the gas) are shown in Fig. 1. Values of the non-dimensional heat-flux ratio Q^*/Q_0^* are plotted at corrected values of S' as defined in Eq. (5).

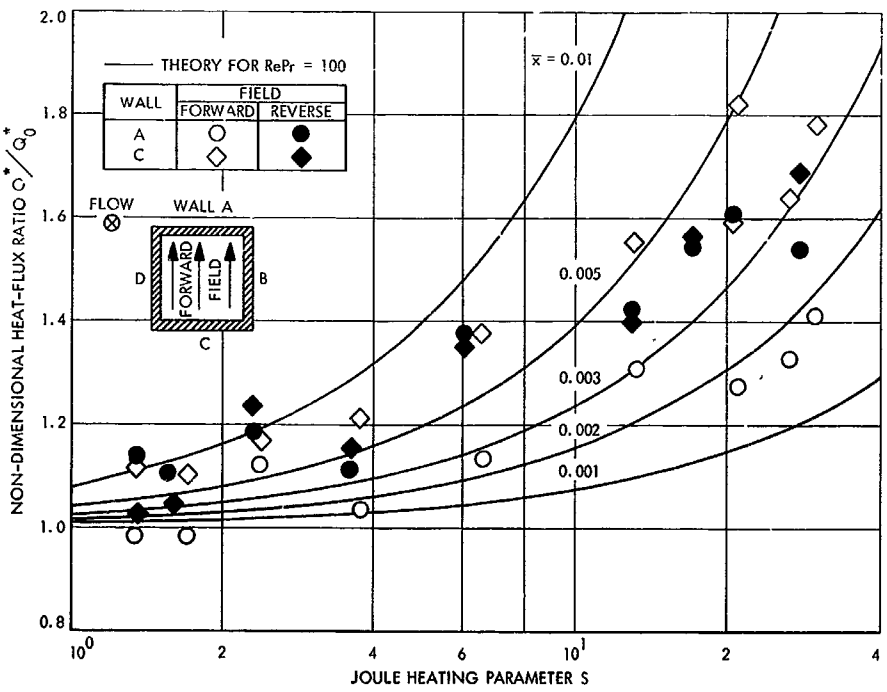

Fig. 1. Non-dimensional heat flux at second segment of test section for subsonic flow, tests 107-18H and -19H

Forward field indicates an applied magnetic field directed vertically upward and vice versa for reverse field In this case, at the highest values of S obtained, $0.25 < \beta_e\beta_i < 0.30$. It is clear that substantial increases in heat transfer occur with an increase in either S or S'. The relatively good agreement between walls A and C for reverse field is noted; the reason data for wall A at forward field are low has not yet been determined.

Also appearing in Fig. 1 are theoretical predictions adapted from Back (Footnote 1). Each curve represents the variation of Q^*/Q_0^* with S for different nondimensional axial distances from the inlet, as defined by $\bar{x} = (x/2a)/RePr$. Although the curves are indicated for $RePr = 100$, they are virtually independent of $RePr$ for values of $RePr$ greater than 50. For these experiments $82 < RePr < 110$. The trend of the data is in rough agreement with the theory. Experimental values of $\bar{x}$ are not known because the "effective" location at which the flow may be considered to begin is not determined. If the "starting" point of the flow is considered to occur at the center of the first segment of the test section (1 in upstream of the location of these data), values of $0.005 < \bar{x} < 0.006$ would be obtained. The agreement between theory and experiment is sufficiently good to be encouraging.

5. Results for a Case of Initially Supersonic Gas Flow

The results of test 107-26H were of interest because large values of S were obtained. This test was considered to be initially supersonic (before applied field) because the bulk equilibrium Mach number was greater than unity, the flow was accelerating, and the axial pressure distributions were unlike those obtained in the subsonic cases. This is demonstrated in Fig. 2, which is a comparison of results for tests 107-18H and -26H; both tests were conducted with a value of mass flow rate $\dot{m} \simeq 0.007$ lb/s.

The effect of the applied magnetic field on static pressure measured at the wall is shown in Fig. 3. These results differ from equivalent results for test 107-18H (see SPS 37-51, Vol. III) in several important ways: (1) peaking of the pressure distribution still occurs but is much less sharp and occurs further upstream than test 107-18H indicates, (2) the relative increase in pressure in the test section is much greater in the supersonic case compared

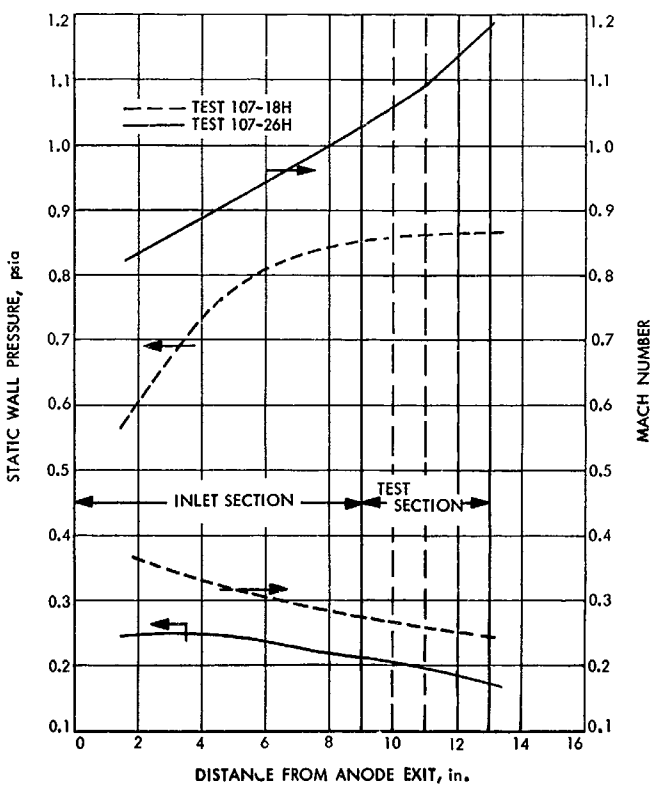

Fig. 2. Comparison of axial distributions of pressure and Mach number for subsonic and supersonic cases with zero applied magnetic field

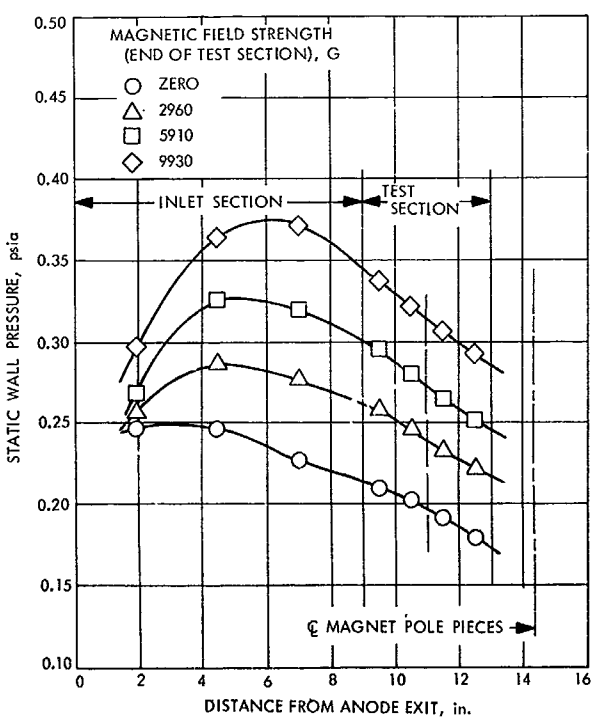

Fig. 3. Effect of magnetic field on axial pressure distribution along side wall B, test 107-26H

to the subsonic case, and (3) the pressure gradient in the test section is somewhat greater in the supersonic case.

Heat-transfer results for this test are shown in Fig. 4 in the same manner as Fig. 1 was depicted; larger values of S' and Q^*/Q_0^* are evident. In this case, the highest values of S obtained were approximately 250, whereas the corresponding values of $1.5 < \beta_e\beta_i < 3.1$ were computed so that S' was markedly less than S at the highest values of the magnetic field. Values of $RePr$ were similar to those obtained in test 107-18H. Trends of the data (Figs. 1 and 4) are similar. In the latter case, a comparison with theory would tend to indicate a higher value of $\bar{x}$ for the supersonic case than for the subsonic case. Again, one low set of data is evident, this time for wall C with reverse field. In contrast to the subsonic case, better agreement between walls is obtained for forward field than for reverse field.

In test 107-26H, for all but the very lowest values of S', the computed bulk values of Mach number throughout the square channel were less than unity; however, the trends of the Mach number were similar to that shown in Fig. 2 so that the nature of the flow is not clear. It does not appear that the results of Fig. 4 are necessarily typical of supersonic flow. It does appear that flow deceleration due to axial Lorentz forces is relatively greater as the value of the initial Mach number (at zero applied magnetic field) is increased.

6. Conclusions

It is now apparent that joule heating due to an applied magnetic field can cause large increases in heat transfer to the walls of a channel in which a weakly ionized gas is flowing. Trends of the non-dimensional heat flux Q^* increase with the joule-heating parameter S as predicted by theory. The largest increase in Q^* obtained to date has been six times that obtained at zero applied field. Despite the short comings of the theory due to its idealized treatment of incompressible slug flow between infinite parallel plates, it appears that the theory does contain the essential features of the consequences of joule heating.

The values of S computed in these experiments are probably too large because of non-scalar behavior of the electrical conductivity that may occur in strong magnetic

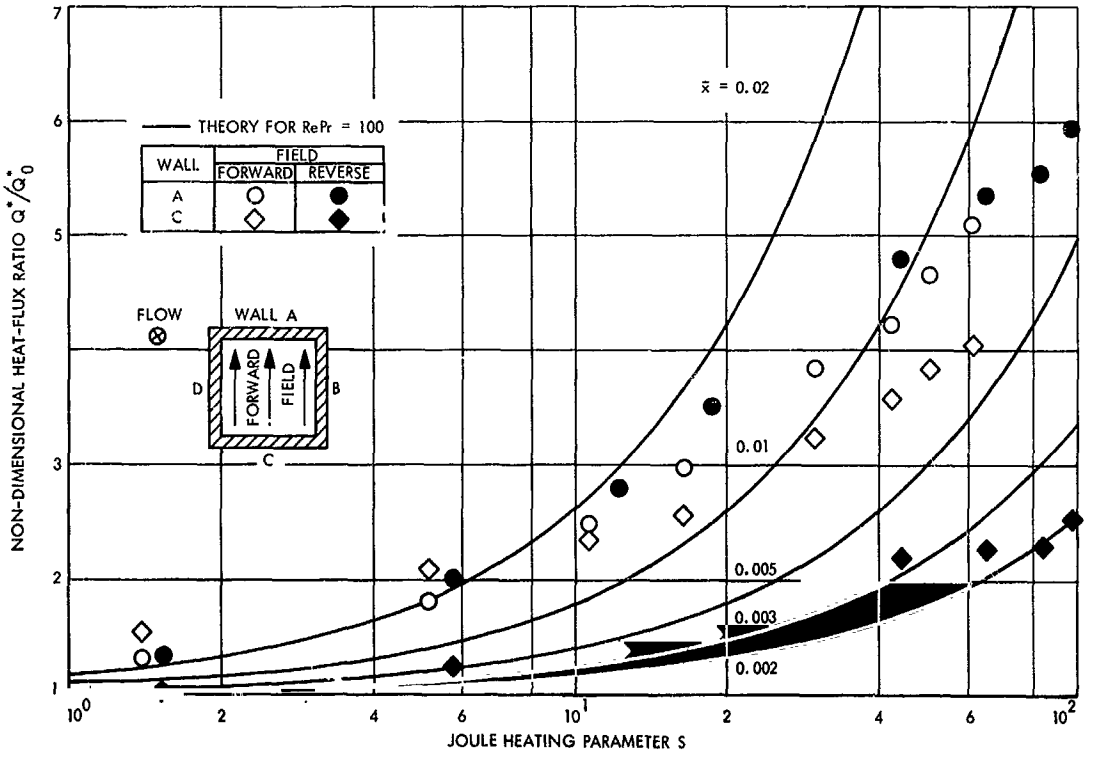

Fig. 4. Non-dimensional heat flux at second segment of test section, test 107-26H; flow initially supersonic at zero magnetic field

fields. Theoretical values of the Hall parameter calculated by usual procedures were much too large to be relevant in the present experimental results; it appears that theoretical values of β_e are one to two orders of magnitude too high. An alternative ion-slip correction suggested in Ref. 2 has been utilized in the form $S' = S/(1 + \beta_e\beta_i)$; this correction yields much more reasonable results since $\beta_i \leq 10^{-2}\beta_e$ in these experiments.

References

1. de Voto, R. S., *Argon Plasma Transport Properties*, Technical Report 217. Stanford University, Department of Aeronautics and Astronautics, Stanford, Calif., Feb. 1965. Also available in *Phys. Fluids*, Vol. 10, pp. 354–364, Feb. 1967.

2. Patrick, R. M., and Brogan, T. R., "One-Dimensional Flow of an Ionized Gas Through a Magnetic Field," *J. Fluid Mech.*, Vol. 5, Part 2, pp. 289–309, 1958.

B. Thermionic Diode Kinetics Experiment,

H. Gronroos

1. Introduction

The thermionic diode kinetics experimental program is part of a continued effort aimed at delineating the problems associated with liquid-metal-cooled thermionic reactors for space powerplant application. This article describes a non-nuclear thermionic reactor system experiment that is now being assembled. The experiment will mainly address itself to the questions of plant dynamics and control. Other parallel evaluations concerned with reactor physics, design and engineering, materials and fabrication, and application studies are not discussed in this article.

The experimental assembly has many features in common with what would be termed a system simulator. However, the assembly is more accurately described as a first step towards a system simulator test. Although the time constants are expected to approximate those existing in a real system, many components are relatively far removed in design from what they probably will be in application.

2. Results of Analytical Investigations

Results of analytical investigations of thermionic reactor system dynamics and control are summarized to clarify the requirements that should be placed on an experimental facility.

a. Open loop stability studies.[2]

(1) The open loop uncontrolled plant is generally inherently stable. However, design modifications to improve marginal stability and increase protection against accidental large reactivity insertions may be required.

(2) The small feedback effects lead to a relatively large change in operating point even for minor perturbations. The self-regulation is inadequate, necessitating active control.

(3) Thermal transients from electric load and reactivity perturbations are damped and can be controlled with conventional controller hardware. This also holds for thermal transients following open circuiting at the reactor terminals. If uncontrolled, this leads to large and fast fuel and emitter temperature increases.

(4) If the cesium pressure is optimized with respect to a given operating point, the characteristic current–voltage curves cross each other. Then, for a given load line, the heat balance characteristic can pass through a maximum and a minimum. Therefore, conditions for self-sustained oscillations can be conjectured for a nuclear reactor application. With a small increase in cesium pressure, at some cost in efficiency, the characteristics are altered sufficiently to prevent such oscillations.

b. Control studies.[3]

(1) Depending on the system application, either constant reactor output voltage control or a specific programmed response control is feasible.

(2) It appears that existing controller hardware technology is sufficient to meet foreseeable controller performance specifications.

(3) A step change in the electric load will cause a voltage spike to occur at the reactor terminals and, therefore, also at the input to the power conditioner. To avoid the spike at the output of the power conditioner, it must be designed to accommodate the spike for the duration of the transient.

The analytical studies have been useful in building up a theoretical understanding of the system behavior but they necessarily employ models that are only approximate

[2]SPS 37-45, Vol. IV, pp. 151–162, and Ref. 1.
[3]References 2 and 3.

descriptions of the physical system. There are considerable difficulties in the analytical formulation, particularly for start-up and shut-down and for cases of large perturbations. In addition, computer constraints limit the feasibility of detailed modeling of the complete system.

3. Motivations and Requirements

The cost of in-pile experiments are high and, at this time, several hardware problems remain to be resolved. A non-nuclear experiment aimed at investigating the dynamics and control will give inputs for the reliable design of nuclear experiments, and also for the design of a reactor prototype. An experiment designed to give data for evaluation of system responses to various perturbations and simulated accidents will aid in the evaluation of various control concepts. Also, predictions from analytical models can be compared with experimental information. Particularly, studies of system behavior off nominal operating conditions, such as part electrical load, diode open and short circuiting, loss of cesium, loss of coolant flow, start-up and shut-down, and prompt criticality, are important before any nuclear application is attempted. In addition, hardware specifications will be placed on a firmer basis and breadboarded system components can be placed in line with power-producing thermionic diodes.

The experimental facility should have the following features:

(1) Flexibility in simulating various controllers and reactor systems in order to accommodate various design concepts, which implies the use of analog and digital computers on line.

(2) Realistic simulation of thermionic diode performance, which implies the use of diodes approximating prototype designs.

(3) Adequate instrumentation and data reduction systems.

(4) The experiment need not comply with weight and volume limitations applicable to a spacecraft design.

(5) A high-current and low-voltage switching unit for introduction of open and short circuits in a diode matrix.

(6) Simulation of the heat-transfer characteristics of the heat-rejection loop in actual systems, which implies the use of liquid-metal coolant for the experimental assembly.

4. Experimental Assembly

To accommodate the desired objectives as closely as possible and still stay within reasonable cost, an experimental approach shown in Fig. 5 was chosen. Up to six cylindrical thermionic diodes may be mounted vertically in a single-channel NaK-cooled test bank enclosed in a vacuum chamber. Each diode is independently heated by electron beam power. The associated cesium reservoir is also controlled independently. The NaK heat-rejection loop is enclosed in a housing under nitrogen cover gas. An NaK to nitrogen heat exchanger carries away the waste heat.

The generated electrical power is fed to an electrical coupling unit that consists of a series of specially developed, high-current, pneumatically actuated, mercury switches connecting copper bus bars. Any desired series or parallel electrical interconnection between the diodes in the test bank may be chosen, as well as open and short circuit conditions.

The power-conditioning equipment transforms the low voltage–high current dc power generated by the test diodes to high voltage–low current dc power. The electric load simulates the load to which a thermionic reactor powerplant would be connected.

An analog computer provides the nuclear reactor simulation. Thermocouple readings from the diodes and the coolant loop are fed into the computer and the electrical analog of temperature coefficients of reactivity is generated along with the neutron kinetics. The computer controls the electron beam heater power supply for the diodes. Various reactor control concepts can be programmed on the analog computer. With this computer it is also possible to compensate the cesium reservoir temperature in a desired manner (e.g., for simulation of integral cesium reservoir temperature variations).

The controls for the experimental facility monitors the experimental parameters and incorporates the safety circuitry.

A number of constraints had to be considered to implement the outlined experimental approach. Due to cost the number of diodes must be limited. Six diodes was considered to be the minimum number from which a meaningful matrix may be formed. Eutectic NaK is the most feasible coolant choice and permits the use of stainless steel as construction material. Relatively large cylindrical diodes should be used. Because of the very large current (500 A at 0.5 V and 1800°C emitter temperature for the

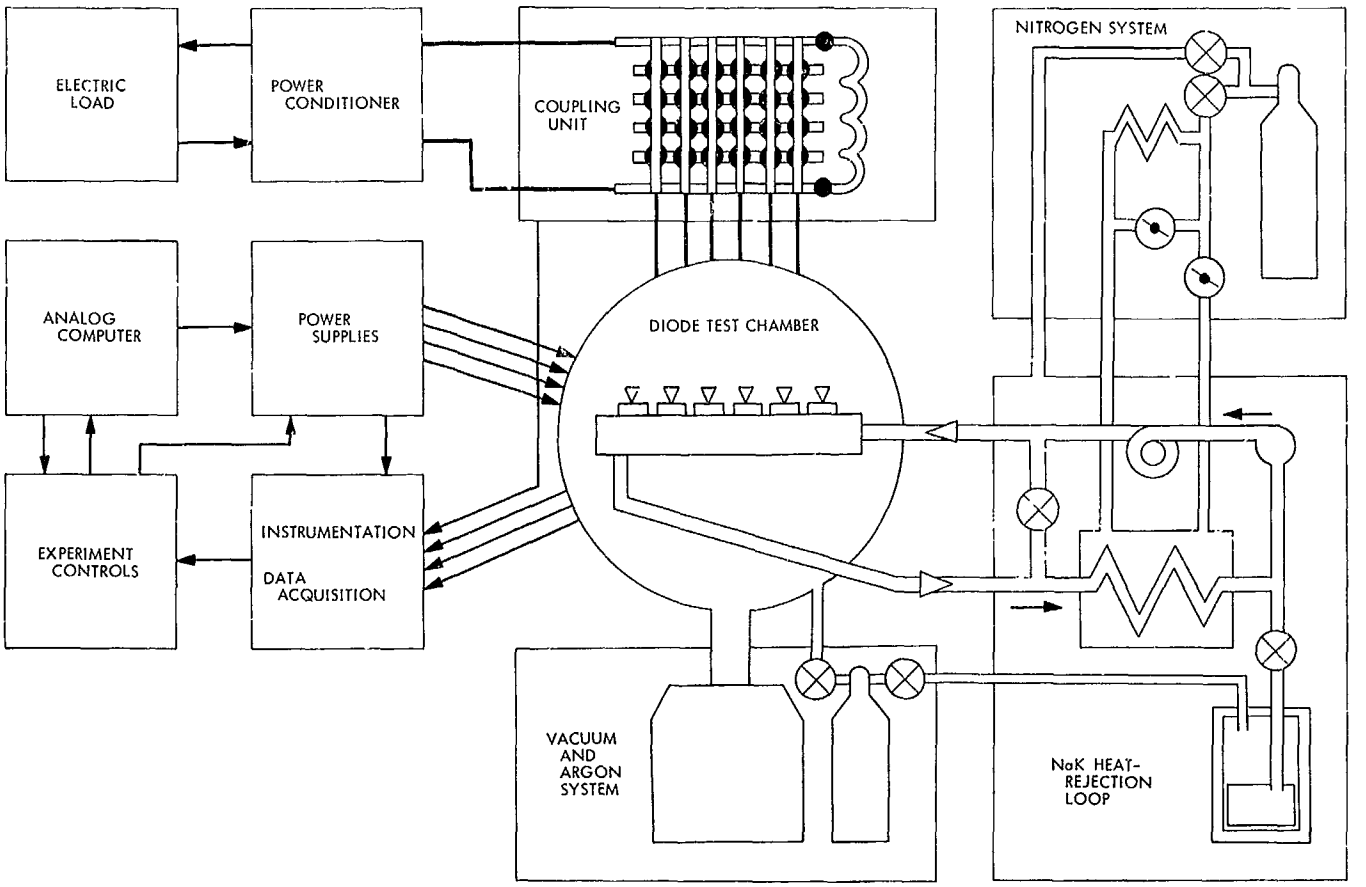

Fig. 5. Schematic of thermionic diode kinetics experiment

chosen diode dimensions), there are difficulties with the switching and power-conditioning units. A separate development effort was necessary for these components.

a. Description of subsystems. The experimental facility consists of two main subsystems: the thermionic diodes with associated equipment and the heat-rejection loop. The analog computer is programmed to give a complete simulation of a thermionic reactor powerplant.

Thermionic diodes. Figure 6 shows a cross-section of a thermionic diode.[4] The emitter is made of rhenium, 0.240 in. thick, 2 in. long, and 0.75 in. outer diameter. The interelectrode gap is 0.010-in. Niobium was chosen as the collector material. The 0.060-in.-thick collector is the inner part of a trilayer construction with 0.060-in. insulator sheath followed by a kovar cladding of 0.020-in. thickness.

The temperature range under normal operating conditions are expected to be: emitter 1900–1500°C, collector 900–600°C, insulator 900–600°C, and cladding 700–600°C. Under open-circuit conditions, the emitter temperature may rise to approximately 2400°C, the collector to 1000°C, and the insulator to 1000°C. The cladding and coolant temperatures will not be allowed to rise appreciably.

Three tungsten–25% rhenium thermocouples are imbedded in the emitter, and three cromel–alumel thermocouples are in the trilayer.

A prototype thermionic diode has been tested and was found to operate well within the specifications. Figure 7 shows some representative test data (Ref. 4).

Test bank, vacuum chamber, and NaK loop. Figure 8 shows the test bank into which the thermionic diodes are installed in the vacuum chamber. All feedthroughs are taken out through one head of the chamber, except for the liquid-metal loop penetrations that come through the side. The frame of the NaK loop outside of the vacuum chamber is shown in Fig. 9. A NaK to nitrogen heat

[4]Manufactured by Thermo Electron Corp., Waltham, Mass.

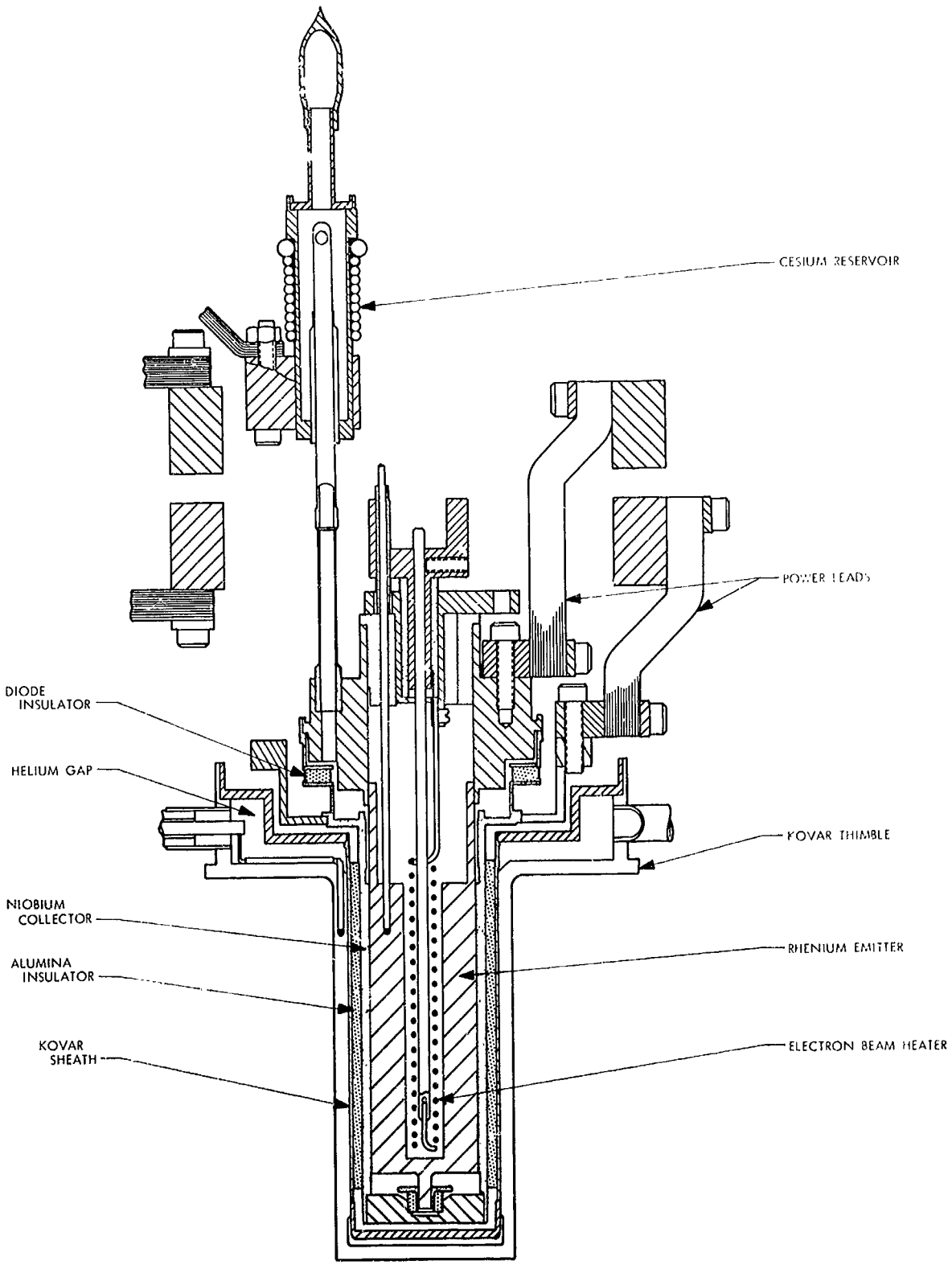

Fig. 6. Cylindrical diode for thermionic diode kinetics experiment

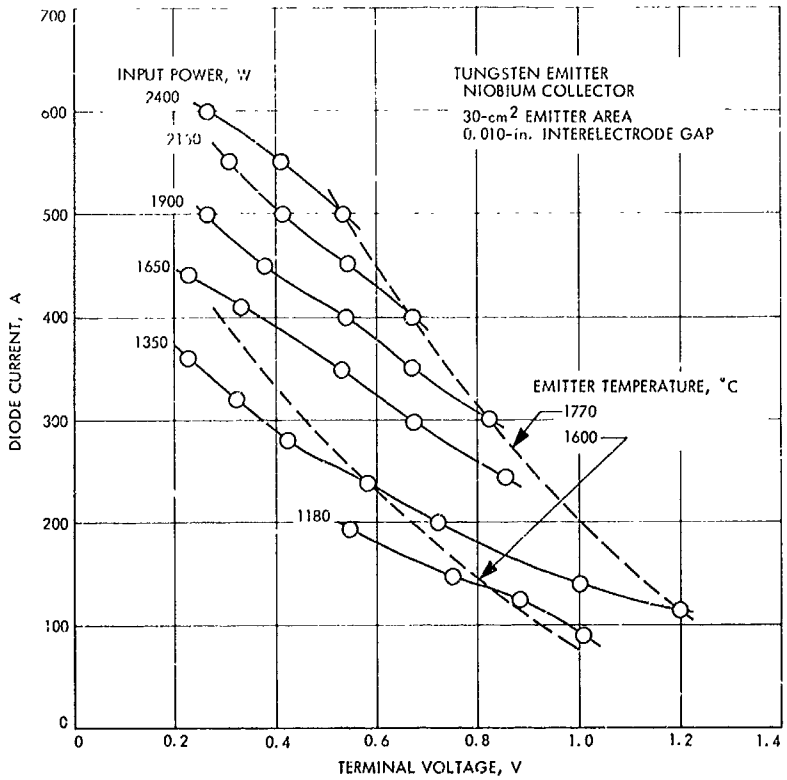

Fig. 7. Test results from prototype diode

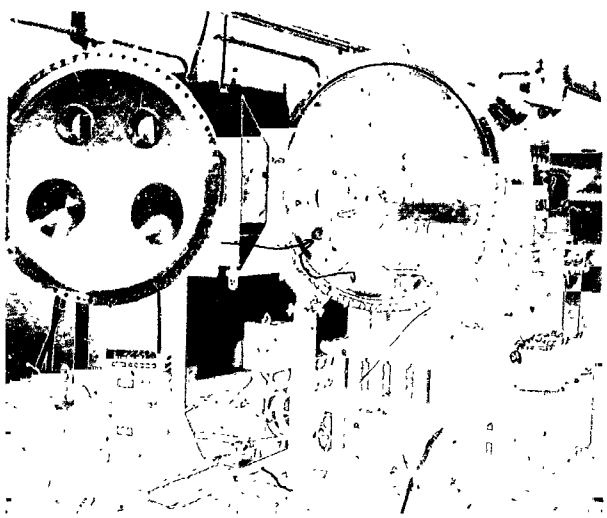

Fig. 8. Test bank and vacuum chamber for thermionic diode kinetics experiment

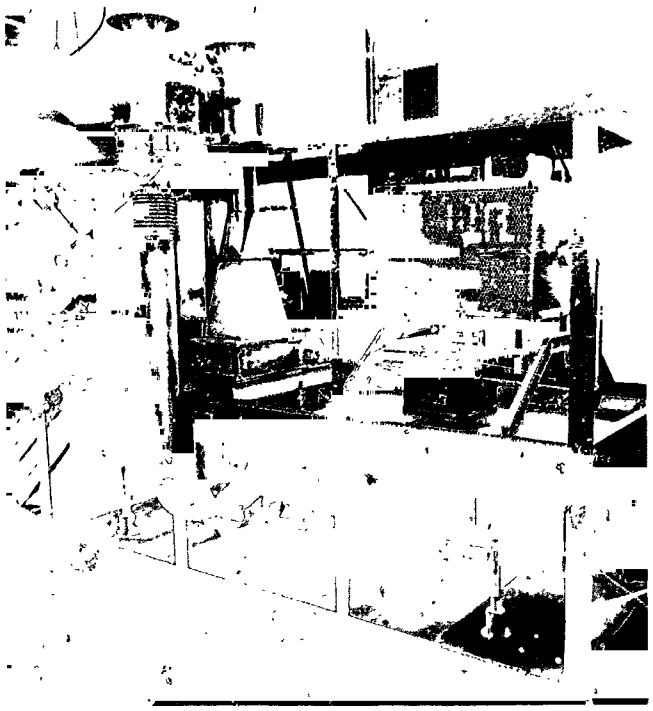

Fig. 9. NaK loop for thermionic diode kinetics experiment

exchanger permits removal of heat up to 25 kW at 1250°F coolant temperature. The electro-magnetic pump has a capacity of 3000 lb/h at 30-psi head, and the preheater provides heat input up to 10 kW. Piping, valves, and test bank are all constructed of 304 stainless steel. Full penetration welded construction is employed. For extra protection, double bellows are used between the vacuum chamber and the external part of the loop.

Diode electric circuitry. The diode electric circuitry consists of copper bus bars leading to the switching unit (Fig. 10). A development effort was necessary to obtain the required high current–low voltage drop (600 A, 5 mV) characteristic for the mercury switches. (This work was also done by the Thermo Electron Corp.) A close-up of the switch is shown in Fig. 11. The circuitry for actuating the switches is such that a selection is made first for the desired coupling pattern, and then all switches are actuated simultaneously.

A special development effort also went into the design of the power conditioner (see *Chapter V-C*). The unit is designed to operate from 1 to 5 V at 700 to 50 A, respectively, and give an output dc voltage of 50 V to a dummy resistive load. A separate cooled resistance coil is connected directly to the switching unit. It is used when the power conditioner is off line.

b. Present status. All major components have been fabricated and assembled. The vacuum tank with accessories, the bank onto which the thermionic diodes are mounted, and the external NaK loop are ready for final joining and welding. All other important auxiliary equipment, such as electron beam heaters with controls, cesium reservoir heaters with controls, and liquid-metal loop-heater power supplies, are available. The instrumentation has been laid out and is being installed. The analog computer has been installed.

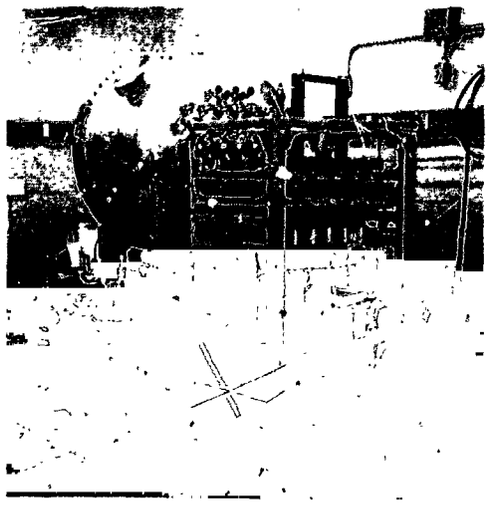

Fig. 10. Coupling unit for thermionic diode kinetics experiment

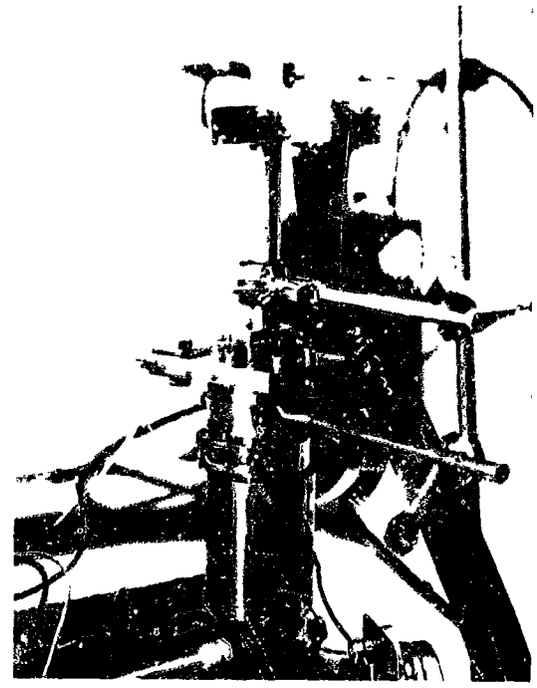

Fig. 11. 600 A pneumatically actuated mercury switch

The various components are now being assembled as a system. The first experiments are expected to begin during fiscal year 1969.

References

1. Schock, A., "Effect of Cesium Pressure on Thermionic Stability," paper presented at the Second International Conference on Thermionic Electrical Power Generation, Stresa, Italy, May 27–31, 1968.
2. Gronroos, H., et al., "A Control System Study for an In-Core Thermionic Reactor," paper presented at the IEEE Thermionic Conversion Specialist Conference, Palo Alto, Calif., Oct. 30–Nov. 2, 1967.
3. Grouroos, H., and Davis, J. P., "Stability and Control Considerations for Thermionic Reactors," paper presented at the Second International Conference on Thermionic Electrical Power Generation, Stresa, Italy, May 27–31, 1968.
4. Peelgren, M., and Speidel, T., "Large Cylindrical Diodes with Rhenium Emitter for Diode Kinetics Experiment," paper presented at the IEEE Thermionic Conversion Specialist Conference, Framingham, Mass., Oct. 21–23, 1968.

C. Liquid–Metal MHD Power Conversion,

D. G. Elliott, D. J. Cerini, and L. G. Hays

1. Introduction

Liquid–metal magnetohydrodynamic (MHD) power conversion is being investigated as a power source for nuclear-electric propulsion. A liquid–metal MHD system has no moving mechanical parts and operates at heat-source temperatures between 1600 and 2000°F. Thus, the system has the potential of high reliability and long lifetime using readily available containment materials such as Nb–1%Zr.

In the MHD cycle being investigated, liquid lithium would be (1) heated at about 150 psia in the reactor or reactor-loop heat exchanger; (2) mixed with liquid cesium at the inlet of a two-phase nozzle, causing the cesium to vaporize; (3) accelerated by the cesium to about 500 ft/s at 15 psia, (4) separated from the cesium; (5) decelerated in an ac MHD generator; and (6) returned through a diffuser to the heat source. The cesium would be condensed in a radiator or radiator-loop heat exchanger and returned to the nozzle by an MHD pump.

2. NaK–Nitrogen Conversion System

The empty-channel electrical tests of the ac generator have been completed. The tests demonstrated the readiness of the instrumentation and electrical control systems for the NaK–nitrogen tests and the ability to set a uniform traveling magnetic field with proper compensation. The only unexpected result was that the core loss,

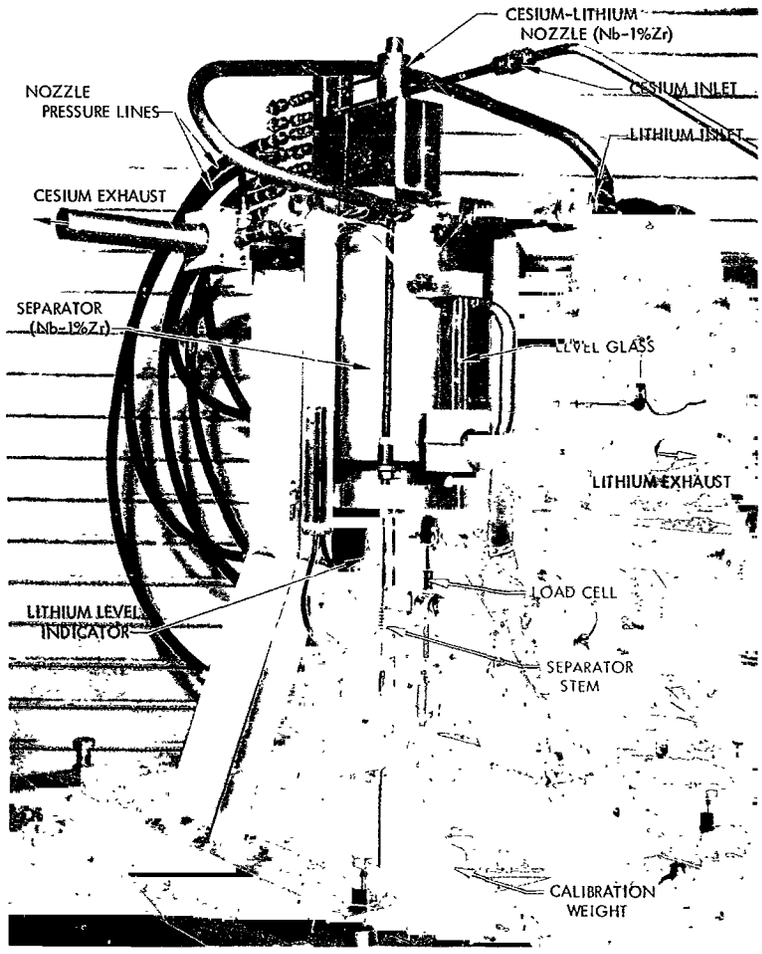

Fig. 12. Cesium–lithium nozzle–separator assembled for hydraulic evaluation

measured at phase currents up to 19 A (rms gap field of 1100 G), was about 5 times the standard value for Hiperco 50. The added loss would reduce the maximum power output from 42 to about 30 kW. The fabrication step causing the high loss will be identified and modified, if possible, in subsequent stators.

Power losses were also measured for the supporting H-frames and for the proposed Hiperco slot plugs. The added core loss due to the H-frames was 6 kW (extrapolated to the intended operating field of 4500 G rms) and was unaffected by annealing and negligibly affected by displacement 1-in. away from the stators. The addition of solid or laminated Hiperco slot plugs increased the core loss by an even larger amount, and also doubled the required coil voltages and produced a nonsinusoidal variation of gap field with time, although the variation of field with distance was smoother. It was decided to employ fiberglass for the H-frames and slot plugs in the NaK tests.

To observe the effect of a conducting sheet in the generator, aluminum plates of various thicknesses were placed in the channel and the exerted force and dissipated power were measured. The values agreed with expected values within the 20% uncertainty of the measurements.

3. Cesium–Lithium Erosion Loop

The auxiliary argon and vacuum systems have been completed. The NaK heat-removal system and controls have been completed and are ready for liquid-metal fill. The control system and console are complete, and control operation is being tested.

Figure 12 shows the two-phase nozzle and separator assembled for water–nitrogen tests. The purpose of the tests is to verify proper operation of the separator and to compare the nozzle thrust measured by the target method (to be used during high-temperature operation) with previous direct measurements (SPS 37-48, Vol. III, pp. 125–129). The best adjustment of the separator exit gap indicated by the tests will be retained in the final welding.

Measurement of the level of 2000°F lithium in the separator discharge chamber will be attempted with a new type of probe shown schematically in Fig. 13. This level indicator operates on the principle that the heat transfer from the liquid phase is much greater than that from the vapor phase. Hence, if the total heat input to an internally

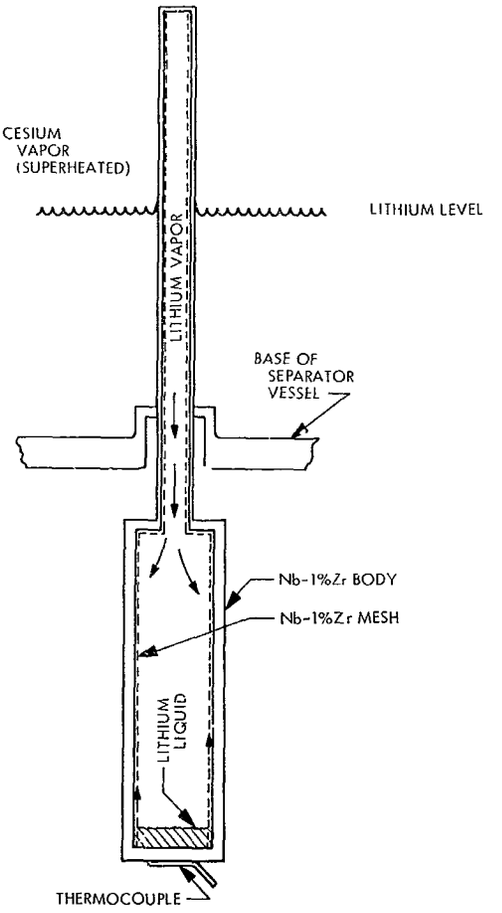

Fig. 13. Differential heat-transfer level indicator for cesium–lithium separator

cooled probe is measured, it will be directly proportional to the length of the probe in contact with the liquid metal. For the probe of Fig. 13, the heat input is transferred by the heat-pipe action of lithium to a section where the heat is rejected by radiation. Since the area of the radiating section is fixed, the temperature of the radiating section is determined by total heat input and, hence, liquid level. The resultant probe is of very simple and rugged construction and provides a reliable, high-level signal (thermocouple output).

The approximate relationship (neglecting heat pipe and wall temperature differences) that holds between liquid level and temperature is

$$\pi d_0 (L_0 - L_l) \bar{h}_v (T_l - T_r) + \pi d_0 L_l \bar{h}_l (T_l - T_r) = A_r \sigma \epsilon (T_r^4 - T_e^4)$$

where

d_o = probe diameter

L_o = probe length

L_l = liquid level

$\bar{h}_v$ = vapor heat-transfer coefficient

$\bar{h}_l$ = liquid heat-transfer coefficient

T_l = liquid temperature

T_r = radiating temperature

T_e = ambient temperature

A_r = radiating area

ϵ = emissivity

σ = Stefan–Boltzmann constant

For the case $\bar{h}_v << \bar{h}_l$,

$$L_l \approx \frac{A_r \sigma \epsilon (T_r^4 - T_e^4)}{\pi d_o \bar{h}_l (T_l - T_r)}$$

Thus, for a fixed geometry, the liquid level is a function of the natural convection coefficient $\bar{h}_l$, the lithium temperature T_l, the ambient temperature T_e, and the radiating temperature T_r. During a test the first three parameters will be nearly constant, and T_r will provide a measure of the level. The calculated relation between lithium level and radiating temperature T_r for the geometry of the separator probe is shown in Fig. 14. This calculation included the effect of wall temperature differences and the variation of $\bar{h}_l$ with L_l. A change in level of 3 in. results in a change in thermocouple output of 100°F. Calibration of the probe at one level will be used to establish the actual operating curve.

The predicted behavior was checked with a similar level indicator at lower temperature with water as the heat-pipe fluid. In this probe the heat rejection from the radiator was accomplished by natural convection. The unit was tested by varying the level of Dow-Therm A heated to 250°F with the result shown in Fig. 15. The measured temperature difference agrees with the calculated value within 15%, and the theoretical variation of temperature with level is followed closely.

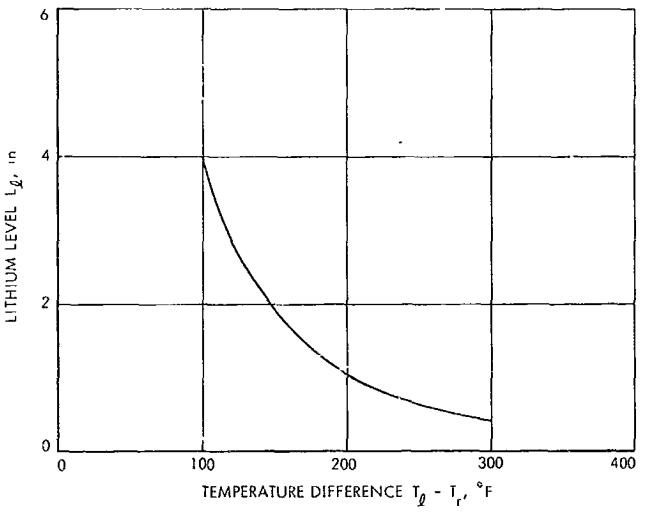

Fig. 14. Lithium level vs temperature difference for separator probe at 2000°F lithium temperature

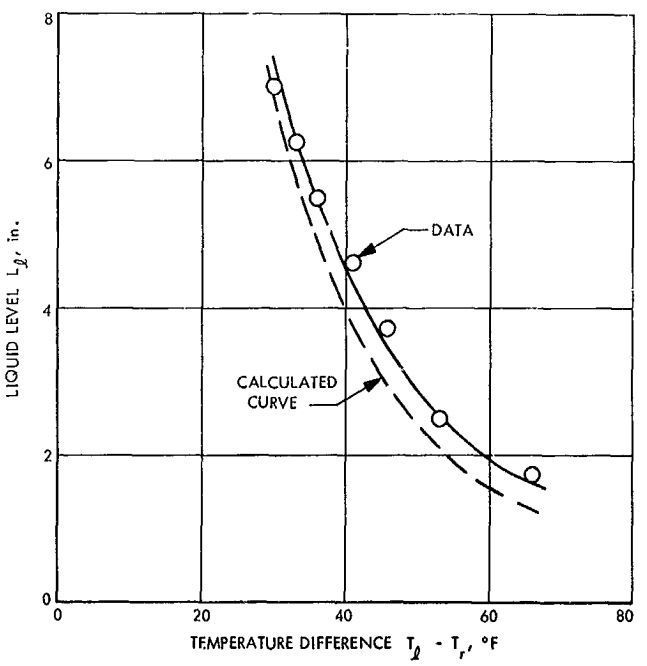

Fig. 15. Comparison of measured and calculated liquid level for differential heat-transfer liquid-level indicator in Dow-Therm A at 250°F

XIV. Liquid Propulsion

PROPULSION DIVISION

A. Combustion Effects in Sprays, *J. Houseman*

1. Introduction

In the area of injector design for liquid-propellant rocket engines, use is made of the experimental data obtained in cold-flow tests with simulated propellants. It is usually assumed that the effects of combustion on impingement and spray formation are small. The mass and mixture ratio distributions in an actual propellant spray are considered to be essentially the same as in a simulant spray.

This article presents experimental data which shows that, under many conditions, this assumption is not valid. This applies particularly to hypergolic propellants. A jet of nitrogen tetroxide impinging upon a jet of hydrazine[1] results in a nonuniform spray in which the oxidizer side is rich in oxidizer while the fuel side is rich in fuel. A sketch of the impingement region is shown in Fig. 1. Since the propellants are considered to be immiscible, liquid phase mixing and chemical reaction take place at the interface between the jets. The formation of gas at the interface prevents mixing of the streams and results in stream separation or "blowing apart" of the jets, which produces a nonuniform spray mixture.

Three mechanisms for stream separation are postulated as follows:

(1) Local boiling of the propellant due to heat released by liquid phase reaction.

(2) Gas evolution due to gaseous products of liquid phase reactions.

(3) Formation of a gas film between the jets due to gas phase reaction.

Theoretical models for these three mechanisms have been developed at JPL and the earliest version (Ref. 1) is shown in Fig. 2. The graph defines a separation-free area on the lefthand side as a function of pressure, propellant injection temperature, and contact time. This contact time is closely approximated by D/V, the orifice diameter divided by the average jet velocity.

An experiment was devised to verify these concepts by measuring the mixture ratio distribution across the spray from an unlike impinging doublet.

[1]Elverum, W. G., and Staudhammer, P., *The Effect of Rapid Liquid-Phase Reactions on Injector Design and Combustion in Rocket Motors*, Aug. 25, 1959 (JPL internal document).

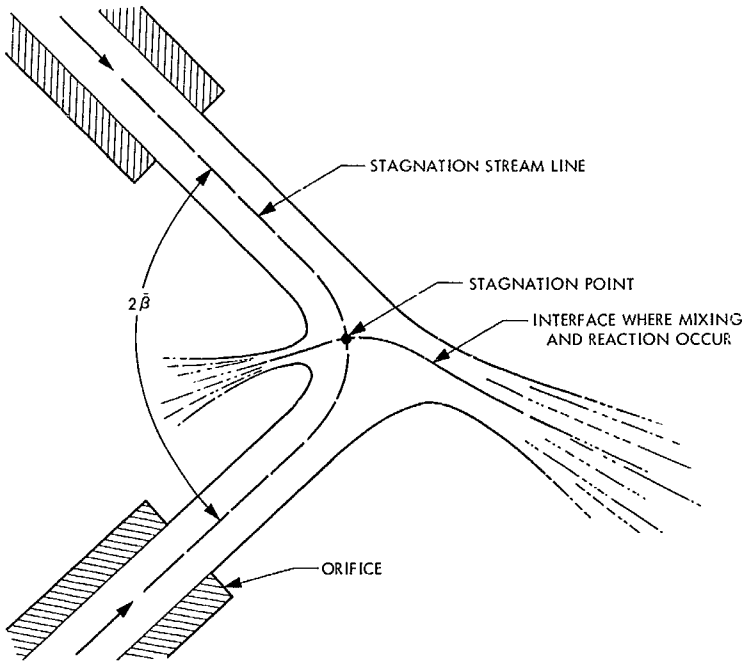

Fig. 1. Jet impingement

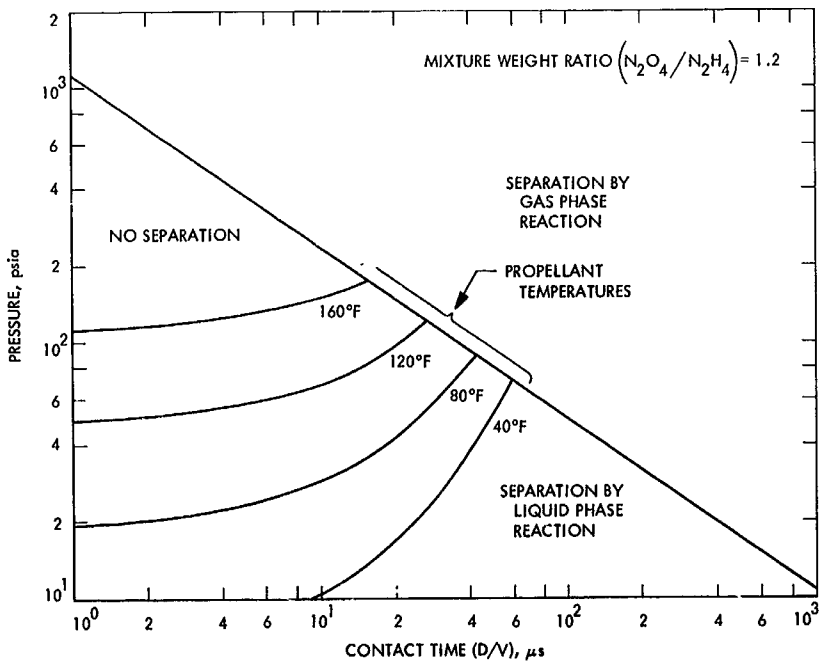

Fig. 2. Stream separation criteria

2. Experimental Procedures

Temperature conditioning of the propellants is achieved by a coil in a water bath, the coil being just ahead of the firing valve. The chamber and sampling probe assembly are shown in Fig. 3. Two sonic orifices and a leak valve in series provide input gas to the quadrupole mass spectrometer.

The gold probe tip extends 0.140 in. upstream of the water-cooled 0.250-in. stainless steel probe to overcome the boundary layer of the tube. Details of the probe are shown in Fig. 4.

In order to determine the mixture ratio at a point, it is only necessary to measure the H_2/N_2 ratio and the O_2/N_2

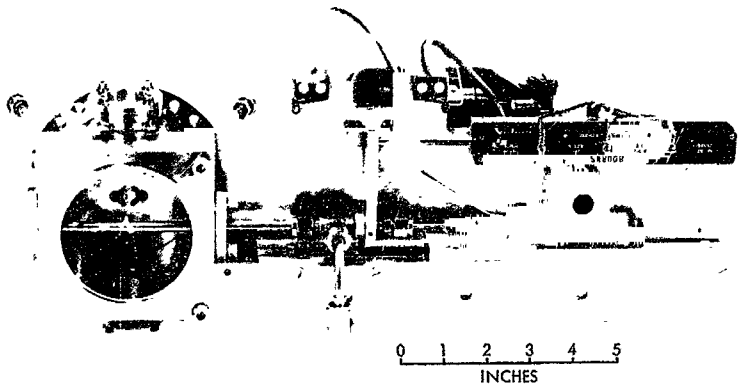

Fig. 3. Engine and sampling probe assembly

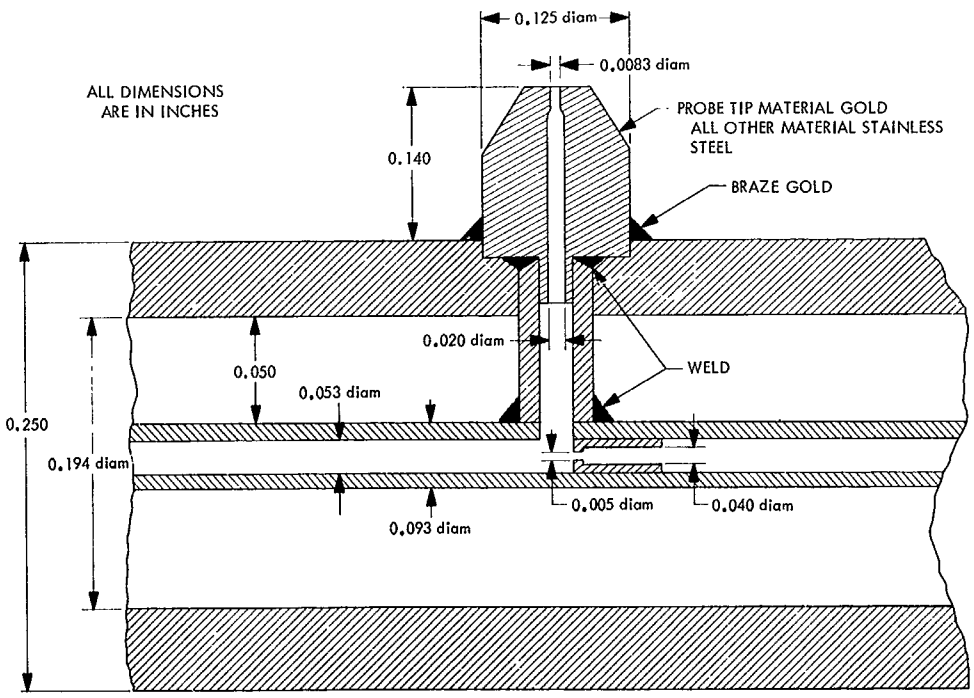

Fig. 4. Probe details

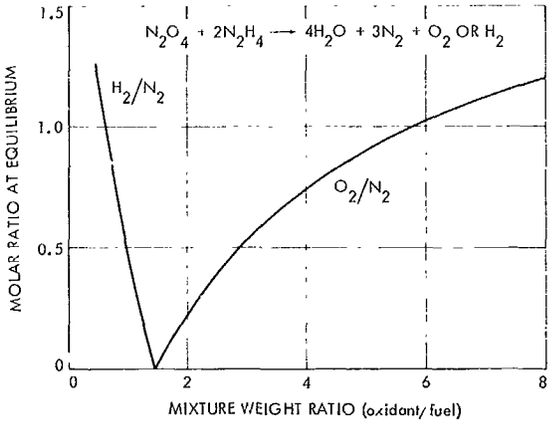

Fig. 5. Equilibrium composition for N_2O_4/N_2H_4 at 300°K

ratio of the sampled gas, as indicated in Fig. 5. The quadrupole mass spectrometer was modified for operation under computer control to obtain a simplified data recording system. As shown in Fig. 6, the normal output consists of a spectrum of up to 50 peaks. The mass numbers are varied from 1 through 50 in a scan by means of a continuous ramp voltage of from 0–10 V. In this experiment, only a few peaks are of interest and only the height of the peak is important, the shape being irrelevant. By setting the ramp voltage at various distinct values corresponding to the top of the peaks of the desired mass numbers, the output of the mass spectrometer will consist of only a few numbers rather than a whole spectrum. This

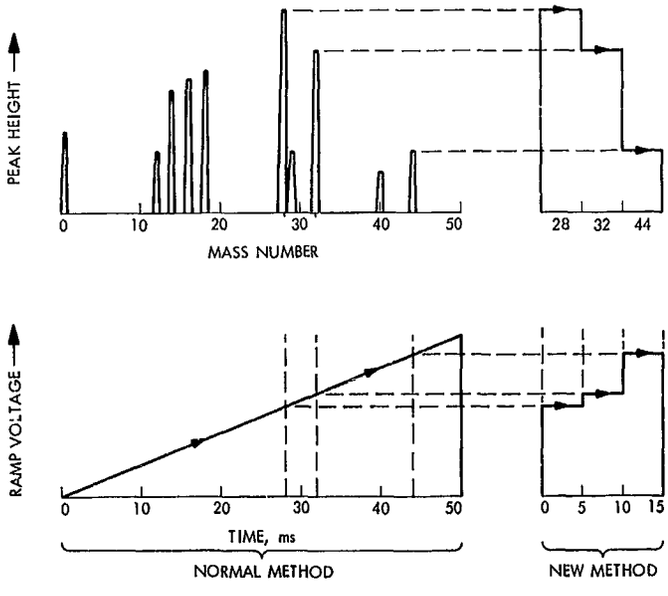

Fig. 6. Mass number selection for quadrupole mass spectrometer

forms the basis for the new method of operation shown on the right side of Fig. 6. A PDP-4 computer was used to generate the ramp voltages to tune the EAI 200 quadrupole to the peaks of interest. The equipment was operated at a scanning speed of one peak per 10 ms.

3. Results

A series of 4.0-s firings was carried out with the probe at different positions in the chamber.

The mixture ratio is definitely nonuniform across the spray and only slightly influenced by injection temperature. Data based on both H_2/N_2 and O_2/N_2 measurements are shown in Fig. 7. The mixture ratio varies from 0.6 on the fuel side to 2.2 on the oxidizer side. The data are plotted on a stream-separation criteria plot in Fig. 8 for comparison with a provisional gas evolution model. Separation occurred at all the points shown. The 140°F points are on the correct, i.e., the separated, side of the 140°F line. However, the 40°F points are on the wrong side of the 40°F line. Comparison with the dashed line for separation by gas-phase reaction shows that all points are in the correct region.

Considerable roughness was experienced with the single unlike doublet. Figure 9 shows chamber pressure

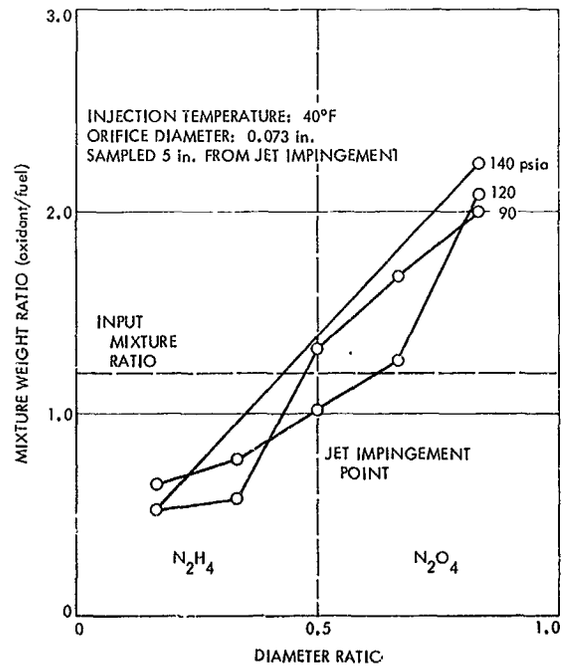

Fig. 7. Stream separation in an unlike doublet

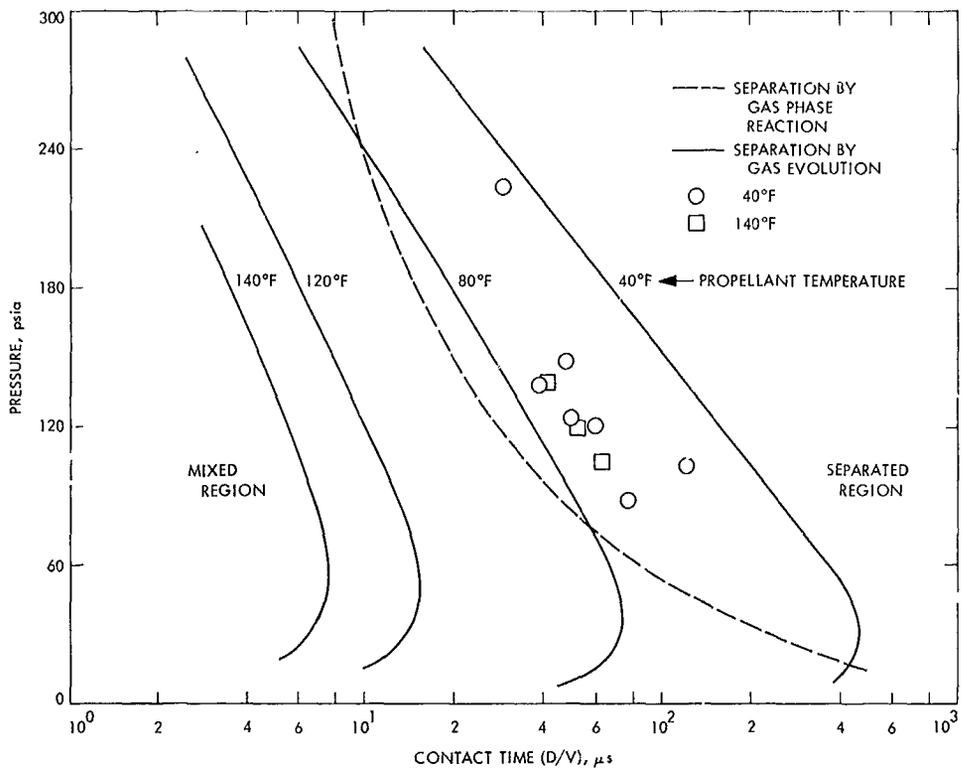

Fig. 8. Gas evolution model

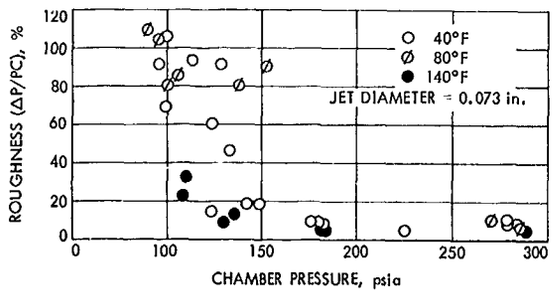

Fig. 9. Roughness with a single unlike doublet

fluctuations (ΔP) up to 100% as a function of average chamber pressures (PC) and propellant temperature. The frequency ranged from 100–250 Hz.

4. Conclusions

The experimental data shows that combustion effects can produce mixture ratio distributions that are significantly different from those obtained in simulated cold-flow tests. When using such cold-flow data, the stream separation criteria should be checked to establish that the element will operate in a non-separated region. This probably applies not only to mixture ratio distributions, but also to mass and drop-size distributions.

Reference

1. Kushida, R., and Houseman, J., *Criteria for Separation of Impinging Streams of Hypergolic Propellants*, Technical Memorandum 33-395. Jet Propulsion Laboratory, Pasadena, Calif., July 15, 1968.